

#### Contents lists available at ScienceDirect

## Acta Materialia

journal homepage: www.elsevier.com/locate/actamat



## Full length article

## Shock-induced two types of $\{10\overline{1}2\}$ sequential twinning in Titanium

Shun Xu <sup>a</sup>, Ping Zhou <sup>b</sup>, Guisen Liu <sup>a</sup>, Dawu Xiao <sup>c</sup>, Mingyu Gong <sup>a</sup>, Jian Wang <sup>a,\*</sup>



- <sup>a</sup> Mechanical and Materials Engineering, University of Nebraska-Lincoln, Lincoln, NE, 68588, USA
- <sup>b</sup> Science and Technology on Surface Physics and Chemistry Laboratory, Jiangyou, 621908, China
- <sup>c</sup> The Institute of Materials, China Academy of Engineering Physics(CAEP), Jiangyou, 621907, China

#### ARTICLE INFO

Article history:
Received 25 September 2018
Received in revised form
7 December 2018
Accepted 9 December 2018
Available online 11 December 2018

Keywords: Titanium Shock loading Twinning EBSD Crystal plasticity

#### ABSTRACT

Shock loading causes complicated twinning processes in Ti and Ti alloys. In this work, two types of  $\{10\overline{1}2\}$  sequential twinning processes are for the first time reported according to electron backscatter diffraction (EBSD) characterization of titanium sheets that are subjected to shock loading. One is described as  $\{11\overline{2}1\} \Rightarrow P \rightarrow \{10\overline{1}2\}$  ( $T_i^{II} \Rightarrow P \rightarrow T_i^{I}$ ), i.e.,  $\{10\overline{1}2\}$  sequential twinning is activated in the parent grain (P) along with  $\{11\overline{2}1\}$  twins. The other is described as  $\{11\overline{2}2\} \Rightarrow \{11\overline{2}4\} \rightarrow \{10\overline{1}2\}$  ( $C_i^l \Rightarrow C_i^{ll} \rightarrow T_h^l$ ), i.e.,  $\{10\overline{12}\}\$  secondary twinning is stimulated inside  $\{11\overline{24}\}\$  twin by co-zone  $\{11\overline{22}\}\$  twin. A statistical analysis according to EBSD characterization reveals the well-defined crystallographic relations between sequential {10 $\overline{1}$ 2} twin variants and the primary/incoming twins, i.e.,  $T_i^{ll} \Rightarrow P \rightarrow T_i^{l}$  or  $T_{i+1}^{l}$  and  $C_i^{l} \Rightarrow C_{i+3}^{ll} \rightarrow C_{i+1}^{l}$  $T_i^l$  or  $T_{i+1}^l$ . We proposed and examined two sequential twinning mechanisms, (i) emissary twinning disconnections at steps along twin boundary for the first case and (ii) shear transformation into the primary twin for the second case, based on dislocation theory and the deformation accommodation ability of the sequential  $\{10\overline{12}\}$  twinning to the shear deformation of the primary/incoming twin. Crystal plasticity modelling is performed to calculate the local stress field associated with the proposed twinning mechanisms. The results demonstrate that the preferred twin variant observed in experiments has the maximum resolved shear stress among the six twin variants. Our work suggests that complicated twinning processes under shock loading obey crystallographic relations according to deformation accommodation ability. The findings from this study can be implemented into meso-/macro-scale crystal plasticity models for predicting mechanical behaviors and texture evolution of polycrystalline aggregates of hexagonal materials.

© 2018 Acta Materialia Inc. Published by Elsevier Ltd. All rights reserved.

### 1. Introduction

Titanium and titanium alloys with the superior strength-to-density ratio, the extraordinary corrosion resistance and the ability to withstand extreme temperatures are widely used in the automotive, aerospace, marine, power generation and offshore industries [1]. Laser shock peening techniques have been used to improve performance of high cost titanium alloy parts in the aerospace industry and other industries [2]. It is of great interest to understand the mechanical response of titanium and titanium alloys in the complex dynamic loading environments that are experienced in these engineering applications. Much effort has been devoted to determining the predominant deformation mechanisms in titanium and titanium alloys over a range of strains and strain

rates [3,4], temperatures [5,6], grain sizes [7], polycrystalline textures [8], etc.

Both dislocation slip and twinning are activated in titanium with a hexagonal close packed structure (HCP) [9]. The easy slip happens along  $\langle a \rangle$  direction on prismatic  $\{10\overline{1}0\}$  and basal  $\{0002\}$  planes [10,11], and they are less dependent on strain rate and temperature. Non-basal  $\langle c+a \rangle$  slip occurs on  $\{10\overline{1}1\}$  and  $\{11\overline{2}2\}$  pyramidal planes [9,12], but the activity relative to other slips and twins is low while increases at large strain [13.14]. Prismatic  $\langle c \rangle$ -type dislocations are occasionally observed at various strain rates and temperatures [15]. It is noted that  $\langle a \rangle$  dislocation on  $\{10\overline{1}2\}$  planes and  $\langle \langle c+a \rangle \rangle$  dislocations on  $\{11\overline{2}2\}$  and  $\{10\overline{1}1\}$  pyramidal planes can be activated [16] under shock loading at strain rate  $10^3$  s<sup>-1</sup> [17,18]. Owing to the low activity of non-basal dislocations, twinning cooperates with and competes against non-basal slips to accommodate deformation along **c**-axis. Twins are classified into two groups, i.e., compression twins and extension twins corresponding to the deformation along c-axis [19,20]. Six types of twins have been

<sup>\*</sup> Corresponding author.

E-mail addresses: wangj6@gmail.com, jianwang@unl.edu (J. Wang).

reported in Ti, three extension twinning modes  $\{10\overline{1}2\}\langle\langle\overline{1}011\rangle\rangle$ ,  $\{11\overline{2}1\}\langle\langle\overline{1}126\rangle\rangle$  and  $\{11\overline{2}3\}\langle\langle\overline{1}122\rangle\rangle$  (referred to as  $T_i^I, T_i^{II}$  and  $T_i^{III}$ , respectively) and three compression twinning modes  $\{11\overline{2}2\}\langle\langle11\overline{2}3\rangle\rangle$ ,  $\{11\overline{2}4\}\langle\langle22\overline{4}3\rangle\rangle$  and  $\{10\overline{1}1\}\langle\langle10\overline{1}2\rangle\rangle$  (referred to as  $C_i^I$ ,  $C_i^{II}$  and  $C_i^{III}$  respectively) [10,11]. The subscript 'i' represents six variants associated with each twinning mode. Among them,  $\{10\overline{1}2\}\langle\langle\overline{1}011\rangle\rangle$  ( $T_i^I$ ) and  $\{11\overline{2}2\}\langle\langle11\overline{2}3\rangle\rangle$  ( $C_i^I$ ) twins are frequently observed [21-24] at room temperature and at any strain rate.  $\{11\overline{2}1\}\langle\langle\overline{11}26\rangle\rangle$  and  $\{11\overline{2}4\}\langle\langle22\overline{4}3\rangle\rangle$  twins are often observed at high strain rate [16,25].  $\{10\overline{1}1\}\langle\langle10\overline{12}\rangle\rangle$  and  $\{11\overline{2}3\}\langle\langle\overline{11}22\rangle\rangle$  twins [26] are occasionally observed.

A considerable amount of work has been devoted to understanding processes of twinning, secondary twinning and twin-twin interactions [16,23,27,28]. Twinning involves nucleation, propagation and growth processes. Conventional understanding of twin nucleation is based on either the pole-mechanisms [29] or the successive dislocation gliding mechanisms [30,31]. Recently, pureshuffle nucleation mechanism is proposed and demonstrated for  $\{10\overline{1}2\}$  twinning [32-34]. Disregarding nucleation mechanisms for various twins, twins propagate or grow through the shear-shuffle mechanisms via twinning disconnections (TDs) [35] which is described by a dislocation  $\boldsymbol{b}$  and a step of height h [36], referred to as  $(\mathbf{b_i}, h_i)$  TD. The subscript i indicates the number of atomic planes. TDs can pile up to form steps and facets that are associated with locally high stress/strain concentration. For example, the steps/ facets along several types of twin boundaries (TBs) have been characterized by using transmission electron microscopy, such as  $\{10\overline{1}0\} | \{0002\} \text{ steps associated with } \{10\overline{1}2\} \text{ twin } [24.32], \{0002\} | \{10\overline{1}0\} | \{10\overline$  $\{\overline{1}013\}$  steps associated with  $\{10\overline{1}1\}$  twin [37],  $\{0002\}$   $\{\overline{11}22\}$  steps associated with  $\{11\overline{2}2\}$  twin and  $\{1\overline{2}10\}||\{1\overline{2}12\}$  steps associated with  $\{11\overline{2}1\}$  twin [38].

When a twin propagates towards and meets with an interface (either grain boundary or twin boundary), the local shear associated with the incoming twin may partially transform into the adjacent crystal by dislocation slips [39,40] or sequential/secondary twinning [41,42]. For example, secondary twin can be activated in a primary twin, resulting in double twin. Under complicated stress conditions, for example of cyclic loading or strain path changes, secondary twinning mode may be the same as or different from the primary twin. Correspondingly, double twins can be grouped into two types, similar double twin (both primary and secondary twins are either compression or extension twins) and dissimilar double twin (one compression twin and the other extension twin). Electron Backscatter Diffraction (EBSD) analysis and transmission electron microscopes (TEM) have revealed six dissimilar double twins in titanium, three compression -> tension double twins:  $\{11\overline{2}2\} \rightarrow \{10\overline{1}2\} (C_i^l \rightarrow T_j^l) [43,44], \{11\overline{2}2\} \rightarrow \{11\overline{2}1\} (C_i^l \rightarrow T_j^{ll}) [45]$  and  $\{11\overline{2}4\} \rightarrow \{10\overline{1}2\}$   $(C_i^{II} \rightarrow T_i^I)$  [45], and three tension  $\rightarrow$  compression double twins  $\{10\overline{1}2\} \rightarrow \{11\overline{2}2\}$   $(T_i^I \rightarrow C_i^I)$  [43],  $\{11\overline{2}1\} \rightarrow .$   $\{11\overline{2}2\}$  $(T_i^{II} \rightarrow C_j^I)$  [46] and  $\{11\overline{2}1\} \rightarrow \{11\overline{2}4\}$   $(T_i^{II} \rightarrow C_j^{II})$  [45]. The symbol ' $\rightarrow$ ' represents twinning, i.e., the former twin is twinned again into the later twin. Associated with formation of double twins, twin-twin boundaries form, subsequently affecting twinning, de-twinning, and slip processes and resulting in increased strain hardening [23,47,48].

Shock loading will create complex twin structures that affect mechanical properties of materials. Exploiting the mechanisms of complex twinning processes and developing corresponding micromechanical models are an essential step to understand the role of complex twinning processes in affecting mechanical behaviour and develop multi-scale material models [49,50]. In this work, we report on two types of sequential twins occurring in titanium under shock loading,  $\{10\overline{1}2\}$  sequential twinning in matrix

along with {11\overline{11}\overline{21}} twins and {10\overline{12}} secondary twinning associated with the interaction between {11\overline{22}} twin and {11\overline{24}} twin. A statistical analysis according to EBSD characterization reveals the well-defined crystallographic relations between sequential {10\overline{12}} twin variants and primary twins. These crystallographic relations are further examined based on the accommodation ability of sequential twinning to the shear deformation resulted by the primary/incoming twins. Correspondingly, we propose two sequential twinning mechanisms (i) emissary twinning disconnections at steps along primary twin boundary and (ii) shear transformation into the primary twin. The feasibility of the two mechanisms is also examined according to dislocation theory and local stress fields that are obtained by a full-field crystal plasticity fast Fourier transform (CP-FFT) approach.

### 2. Experimental methods

An extruded pure titanium rod (99.995 wt %) with a diameter and length of 6.3 mm was annealed in a vacuum of  $10^{-4}$  Pa at  $800 \, ^{\circ}$ C for 1 h and cooled in the furnace. High strain rate (~2600s<sup>-1</sup>) compression was applied at room temperature by using a split Hopkinson pressure bar (SHPB) device. Compression direction was along the axial direction with a final strain of 0.066. The strain is controlled by a strain-stopper ring mounted on the outer circumference of sample. The strain-stopper ring was set with an inner diameter of 6.85 mm, an outer diameter of 10 mm and a length of 5.88 mm to ensure that the radial deformation of the sample is free from constraint and the axial deformation reaches the expected strain. The contact regions among sample, SHPB and strain-stopper ring were lubricated by Vaseline to reduce friction. There is no plastic deformation on the strain-stopper ring because it is made of spring steel with high yielding strength around 1.4 GPa. After compression, the central region of longitudinal cross section of the deformed sample, processed by low-speed diamond saw cutting was ground by SiC paper from grit 800# to 4000#, then polished for 30min using colloidal silica, and finally etched for 2-5 s by Kroll reagent (volume ratio of HF: HNO3: H2O equals to 2:6:97). EBSD measurements were conducted in a Sirion 200 scanning electron microscopy (SEM) equipped with an EDAX/TEAM data acquisition system. The operation was done at 20 kV with a step size of 0.3 µm. The original EBSD data was analysed with software TSL OIM Analysis 7.

#### 3. Results

#### 3.1. Twin structures under shock loading

Twinning induced by shock loading has been extensively studied in structural metals, causing complicated structure evolution in the material [51,52] because of complex stresses, compressive deformation and subsequent tensile deformation. Fig. 1a shows a typical EBSD map of the deformed sample. Four twin modes,  $\{10\overline{1}2\}$  $(T_i^l)$ ,  $\{11\overline{2}1\}$   $(T_i^{ll})$ ,  $\{11\overline{2}2\}$   $(C_i^l)$  and  $\{11\overline{2}4\}$   $(C_i^{ll})$  twins are observed except for  $\{11\overline{2}3\}(T_i^{III})$  and  $\{10\overline{1}1\}$   $(C_i^{III})$  twins. The next-neighbor grain-to-grain misorientation corresponding to Fig. 1a is shown in Fig. 1b. The peaks at  $\sim 35^{\circ}$ ,  $\sim 64^{\circ}$ ,  $\sim 77^{\circ}$  and  $\sim 87^{\circ}$  are attributed to the formation of  $\{11\overline{2}1\}$ ,  $\{11\overline{2}2\}$ ,  $\{11\overline{2}4\}$  and  $\{10\overline{1}2\}$  twins, respectively. According to the area under the peak associated with each twin mode,  $\{11\overline{2}2\}$  twins and  $\{10\overline{1}2\}$  twins account for the largest proportion,  $\{11\overline{2}1\}$  twins also take up much proportion, and  $\{11\overline{2}4\}$ twins contribute to a small fraction. This seems a general distribution feature in many grains. In addition, other peaks may be associated with twin-twin boundaries. For example,  $\{10\overline{1}2\}$  co-

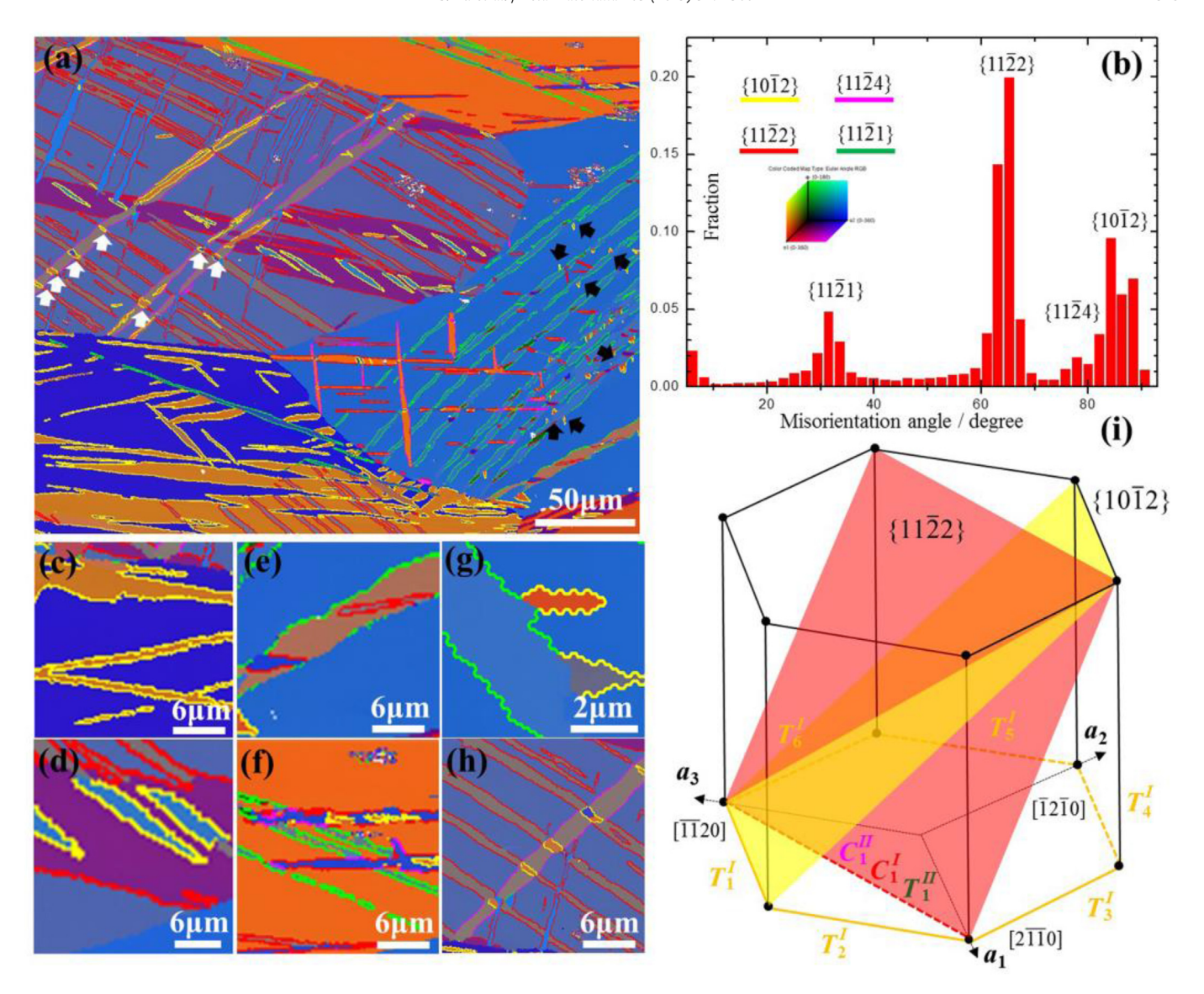


Fig. 1. (a) A typical EBSD map of the deformed sample. Different colors are used to depict the twin boundaries: yellow for  $\{10\overline{1}2\}$ , pink for  $\{11\overline{2}4\}$ , red for  $\{11\overline{2}2\}$  and green for  $\{11\overline{2}1\}$ . (b) The grain-to-grain misorientation angle distribution corresponding to the EBSD map. Specific microstructures are zoomed in (c) twin-twin interactions, (d) compression-tension double twin, (e) tension-compression double twin, (f)  $\{11\overline{2}1\}$  tension twin and  $\{11\overline{2}2\}$  compression twin in one grain, (g)  $\{10\overline{1}2\}$  twins along  $\{11\overline{2}1\}$  twin boundaries, and (h) secondary twins associated with twin-twin interactions. (i) The crystallography of twins, showing the relations among twin modes and twin variants. (For interpretation of the references to color in this figure legend, the reader is referred to the Web version of this article.)

zone twin-twin boundaries could result in a peak around  $\sim$ 7 $^{\circ}$  [28].

Corresponding to the crystallography of twins in titanium, specific colors are used to depict twin boundaries in Fig. 1a, i.e., green lines for  $\{11\overline{2}1\}$  twin boundaries, yellow lines for  $\{10\overline{1}2\}$ , red lines for  $\{11\overline{2}2\}$  and pink lines for  $\{11\overline{2}4\}$ . These twins form complicated microstructures, such as individual (or primary) twins, sequential twins, twin-twin junctions, and double twins. Sequential twin corresponds a twin that is triggered off due to shear transformation associated with dislocation-boundary or twinboundary interactions. The newly formed twin grows in the matrix or a twin. When sequential twinning occurs in one pre-existing twin, the sequential twin is also called secondary twin. Pre-existing twin and secondary twin thus form so-called double twin. Twintwin junctions form associated with twin-twin interactions. For example, Fig. 1c shows twin-twin junctions associated with  $\{10\overline{1}2\}$ twins, which is extensively reported in hexagonal metals [28,53]. Fig. 1d shows compression-tension  $\{11\overline{2}2\} \rightarrow \{10\overline{1}2\}$  double twins,

which is the most popular double twin in titanium [44]. Fig. 1e shows tension-compression  $\{11\overline{2}1\} \rightarrow \{11\overline{2}2\}$  double twins, which is popular in shocked titanium [46]. In addition,  $\{11\overline{2}1\}$  tension twins and  $\{11\overline{2}2\}$  compression twins are activated in the same grain (Fig. 1f), implying the change in stress state during shock loading.

Besides these twin structures, two types of twin structures are for the first time noticed. Fig. 1g shows two small  $\{10\overline{1}2\}$  ( $T_j^I$ ) twins that are activated in the parent (P) grain along  $\{11\overline{2}1\}$  ( $T_i^I$ ) twin boundary. For convenience in description of such twinning process,  $\{11\overline{2}1\}$  twins are referred to as primary twin while  $\{10\overline{1}2\}$  twins are called sequential twin according to their volumes and geometry characters. Such a twinning process is described as  $\{11\overline{2}1\} \Rightarrow P \rightarrow \{10\overline{1}2\}$  or  $T_i^I \Rightarrow P \rightarrow T_j^I$ . The other sequential  $\{10\overline{1}2\}$  twinning happens when incoming  $\{11\overline{2}2\}$  twin interacts  $\{11\overline{2}4\}$  primary twin. A double twin structure,  $\{10\overline{1}2\}$  secondary twin inside  $\{11\overline{2}4\}$ 

primary twin, forms as shown in Fig. 1h. The twinning process is described as  $\{11\overline{2}2\} \Rightarrow \{11\overline{2}4\} \rightarrow \{10\overline{1}2\}$  or  $C_i^I \Rightarrow C_j^{II} \rightarrow T_k^I$  for distinguishing it from the conventional description of double twinning. The symbol ' $\Rightarrow$ ' represents 'interacting', i.e., the former twin (incoming twin) interacts the later crystal (primary twin). Here the later crystal is  $C_j^{II}$  twin. The symbol ' $\rightarrow$ ' represents 'twinning' where the former crystal is twinned into the later twin. Here the former crystal is  $C_i^{II}$  twin.

For the convenience in describing crystallographic relations among various twin modes and their variants, we define the relations among the subscripts "i" of twin variants associated with twin modes  $T_i^l, T_i^{ll}, C_i^l$  and  $C_i^{ll}$ . As shown in Fig. 1i, the zone axis of  $T_i^l$  twin variant is parallel to  $\langle <11\overline{2}0 \rangle >$  (or a) according to the crystallography of an HCP structure. We define the zone axis of  $T_1^l$  along  $\textbf{a}_1$ . The co-zone twin variant  $T_4^l$  thus adopts the zone axis along  $-\textbf{a}_1$ . The zone axis of  $T_i^{ll}, C_i^l$  and  $C_i^{ll}$  twin is parallel to  $\langle <10\overline{1}0 \rangle >$ . We define the zone axis of  $T_i^{ll}, C_i^l$  and  $C_i^{ll}$  twins along the vector  $[\textbf{a}_1-\textbf{a}_3]$ , which is the resultant vector of the two zone axes of  $T_1^l$  and  $T_2^l$ . The other variants "i" can be obtained by rotating the 1st variant  $(i-1)\times 60$  degrees about the [0001] axis. The zone axis of twin variant  $T_{i}^{ll}, C_i^{ll}$  and  $C_i^{ll}$  is thus equal to the sum of the zone axes of the  $T_i^{ll}$  and  $T_{i+1}^{ll}$  variants.

## 3.2. Characteristic of $T_i^{II} \Rightarrow P \rightarrow T_i^I$ twinning

 $T_i^{II} \Rightarrow P \rightarrow T_j^I$ twin structures are classified into three types according to the misorientation between {11 $\overline{2}$ 1} and {10 $\overline{1}$ 2} twins. Take  $T_1^{II}$  for example, six {10 $\overline{1}$ 2} twins exhibit three misorientation

angle/axis pairs with  $T_1^{II}$  twin as listed in Table 1, i.e., Type A ( $T_1^{II}$  and  $T_2^{II}$ ): 66.5° around  $\langle <15\ \overline{5}\ \overline{10}\ 3 \rangle >$ , Type B ( $T_3^{II}$  and  $T_6^{II}$ ): 89.5° around  $\langle <\overline{8}\ \overline{4}\ 12\ 3 \rangle >$  and Type C ( $T_4^{II}$  and  $T_5^{II}$ ): 60.0° around  $\langle <66\ \overline{19}\ \overline{47}\ 14 \rangle >$ . Correspondingly, Type A sequential twinning can be described as  $T_i^{II} \Rightarrow P \rightarrow T_i^{II}$  and  $T_{i+1}^{II}$ , Type B as  $T_i^{II} \Rightarrow P \rightarrow T_{i+2}^{II}$  and  $T_{i+5}^{II}$  and Type C as  $T_{i+3}^{II} \Rightarrow P \rightarrow T_{i+3}^{II}$  and  $T_{i+4}^{II}$ .

Fig. 2a shows a typical EBSD map containing many  $T_i^{II} \Rightarrow P \rightarrow T_i^{II}$ twin structures. A region outlined by the black box is magnified in Fig. 2b. Twin modes are distinguished by the color of the TBs. Green and yellow contours represent  $\{11\overline{2}1\}$  and  $\{10\overline{1}2\}$  twins, respectively. The relation between the subscripts "i" and "j" of twin variants is identified by using a pole figure. The pole figure is associated with the sample frame, i.e., X || [100], Y || [010], Z || [001]. Firstly, we project six twinning planes of the parent grain in the pole figure. Secondly, we project six twinning planes of a twin domain in the pole figure. The coincided spot in the pole figure indicates the twin variant. For example to identify the  $\{11\overline{2}1\}$  and  $\{10\overline{12}\}\$  twin variants as labelled by black arrows in Fig. 2b, the pole figure of the  $\{11\overline{2}1\}$  twin planes in Fig. 2c reveals that the projections of  $(11\overline{2}1)$  twinning plane in the grain and the twin closely coincide as outlined by the light blue circle. This twin is determined to be  $T_3^{II}$  variant. Fig. 2d is the pole figure of  $\{10\overline{1}2\}$  planes in the matrix and two twin variants.  $\{10\overline{1}2\}$  twin planes in the matrix are represented by the black dots,  $\{10\overline{1}2\}$  twin planes in the two twins are denoted by the blue squares and red stars. The two twins are determined to be  $T_3^l$  and  $T_4^l$  variants. They nucleate at twin

**Table 1** The misorientation angle/axis pairs for  $\{11\overline{2}1\} \Rightarrow P \rightarrow \{10\overline{1}2\}$  twins,  $\{11\overline{2}2\} \Rightarrow \{11\overline{2}4\} \rightarrow \{10\overline{1}2\}$  twins and  $\{11\overline{2}4\} \rightarrow \{10\overline{1}2\}$  double twins.

G: (10 <u>1</u> 2)	$(11\overline{2}1) \Rightarrow P \rightarrow \{10\overline{1}2\}$		$(11\overline{2}2) \Rightarrow (\overline{11}24) \rightarrow \{10\overline{1}2\}$		$(11\overline{2}4) \rightarrow \{10\overline{1}2\}$	
Six {1012}	Туре	Axis/angle	Туре	Axis/angle	Type	Axis/angle
(10 <u>1</u> 2) [ <u>1</u> 011]	$T_i^{II} \Rightarrow P \rightarrow T_i^I$ (Type A)	<15 <del>5</del> <del>10</del> 3> 66.5°	$C_i^I \Rightarrow C_{i+3}^{II} \rightarrow T_i^I$ (Type A)	<\bullet{9546} 33.6°	$C_{i+3}^{II} \to T_i^I$ (Group III)	<\overline{13\overline{26}} 39 4> 89.5°
$\begin{array}{c} (01\overline{1}2) \\ [0\overline{1}11] \end{array}$	$T_i^{II} \Rightarrow \mathbf{P} \to T_{i+1}^I$ (Type A)	<15 <del>5</del> <del>10</del> 3> 66.5°	$C_i^I \Rightarrow C_{i+3}^{II} \rightarrow T_{i+1}^I$ (Type A)	<45 <del>96</del> > 33.6°	$C_{i+3}^{II} \rightarrow T_{i+1}^{I}$ (Group III)	<\overline{13\overline{26}} 39 4> 89.5°
$\begin{array}{c} (\overline{1}102) \\ [1\overline{1}01] \end{array}$	$T_i^{II} \Rightarrow P \rightarrow T_{i+2}^{I}$ (Type B)	<\bar{8} \bar{4} 12 3> 89.5°	$C_{i}^{I} \Rightarrow C_{i+3}^{II} \rightarrow T_{i+2}^{I}$ (Type B)	<\overline{14 9 5 1>} 67.1°	$C_{i+3}^{II} \rightarrow T_{i+2}^{I}$ (Group II)	<7 20 <del>27</del> <del>20</del> > 44.3°
$\begin{array}{c} (\overline{1}012) \\ [10\overline{1}1] \end{array}$	$T_i^{II} \Rightarrow P \rightarrow T_{i+3}^{I}$ (Type C)	<66 19 47 14> 60.0°	$C_i^I \Rightarrow C_{i+3}^{II} \rightarrow T_{i+3}^I$ (Type C)	<3 19 16 1> 84.3°	$C_{i+3}^{II} \rightarrow T_{i+3}^{I}$ (Group I)	<11 <del>23</del> > 39.5°
$\begin{array}{c} (0\overline{1}12) \\ [01\overline{1}1] \end{array}$	$T_i^{II} \Rightarrow P \rightarrow T_{i+4}^{I}$ (Type C)	<66 19 47 14> 60.0°	$C_{i}^{I} \Rightarrow C_{i+3}^{II} \rightarrow T_{i+4}^{I}$ (Type C)	<16 <del>19</del> 3 1> 84.3°	$C_{i+3}^{II} \rightarrow T_{i+4}^{I}$ (Group I)	<11 <del>23</del> > 39.5°
(1 <u>1</u> 02) [ <u>1</u> 101]	$T_i^{II} \Rightarrow P \rightarrow T_{i+5}^{I}$ (Type B)	<\bar{8} \bar{4} 12 3> 89.5°	$C_i^I \Rightarrow C_{i+3}^{II} \rightarrow T_{i+5}^I$ (Type B)	<5 9 <del>14</del> <del>1</del> > 67.1°	$C_{i+3}^{II} \rightarrow T_{i+5}^{I}$ (Group II)	<7 20 <del>27</del> <del>20</del> > 44.3°

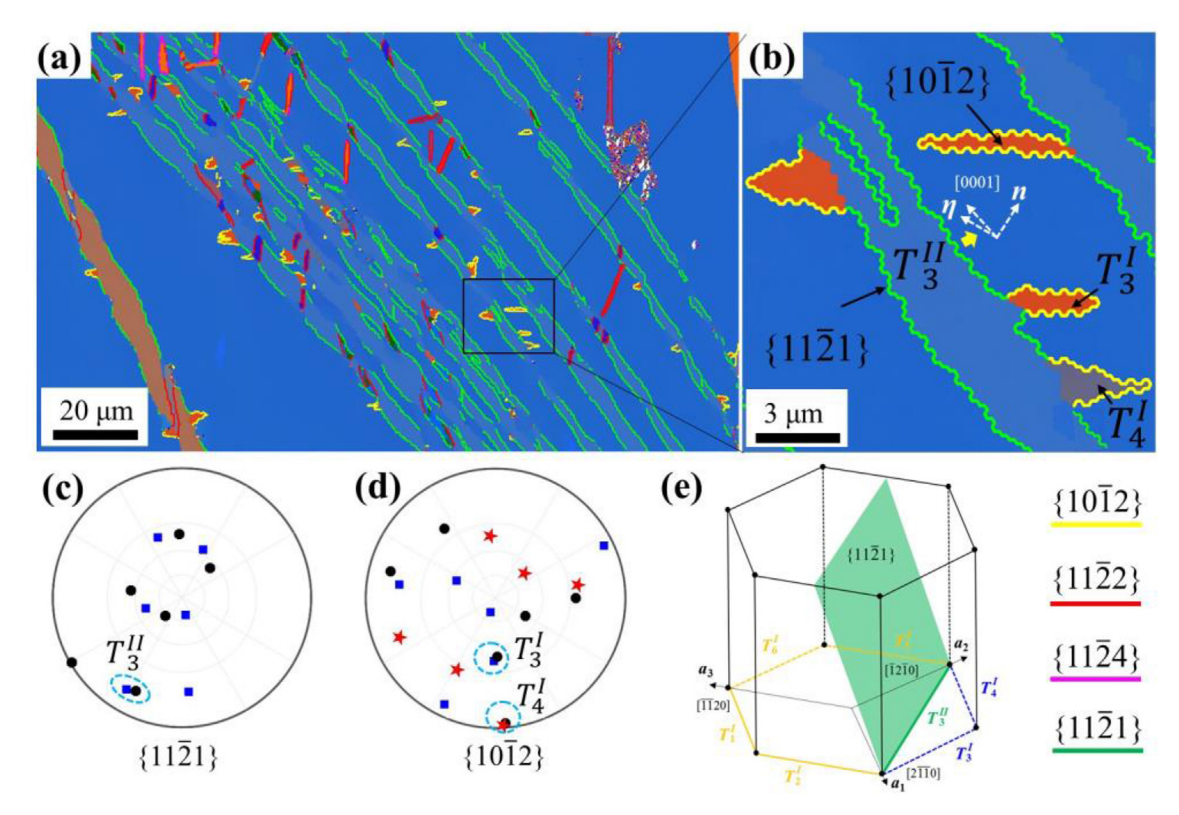


Fig. 2. (a) EBSD characterization of  $T_3^{IJ} \Rightarrow P \rightarrow T_3^{IJ}$  or  $T_4^{IJ}$  twinning planes and (d)  $\{10\overline{12}\}$  twinning planes. (e) The crystallography of  $T_3^{IJ}$ ,  $T_3^{IJ}$  and  $T_4^{IJ}$  twins.

boundaries of the  $T_3^{II}$  and grow in the parent grain. The crystallographic relation between the  $\{11\overline{2}1\}$  twin and two  $\{10\overline{1}2\}$  twin variants is described as  $T_3^{II} \Rightarrow P \rightarrow T_3^{II}$  or  $T_4^{II}$ . The shear direction  $(\eta)$  of the  $T_3^{II}$  twin is projected into the EBSD observation plane as labelled with white arrows in Fig. 2b, showing that the trace of the stimulated  $T_3^{II}$  and  $T_4^{II}$  twin planes have an obtuse angle with respect to the shear direction  $\eta$ . Fig. 2e shows the crystallographic relation between  $T_3^{II}$  twin and  $T_3^{II}$  or  $T_4^{II}$  twin. The zone axis of  $T_3^{II}$  twin is along  $[\overline{1}100]$ , which is equal to the vector summation of the two zone axes of  $T_3^{II}$  and  $T_4^{II}$  twins (highlighted in blue). More importantly, twinning shear associated with  $T_3^{II}$  and  $T_4^{II}$  twins is mirror symmetry about the shear plane of  $T_3^{II}$  twin. Thus,  $T_3^{II}$  and  $T_4^{II}$  twins are equivalent with respect to the resulted shear on the shear plane of  $T_3^{II}$  twin.

We identified 531 {10 $\overline{1}2$ } twins at the TBs of 103 {11 $\overline{2}1$ } twins that are observed in eight grains. Type A twins  $T_i^{II} \Rightarrow P \rightarrow T_i^I$  and  $T_{i+1}^I$  take 474 out of 531 (89.3%), Type C twins take 55 out of 531 (10.3%) and Type B has only two (0.4%). The apparent prevalence of Type A twins will be discussed in details in the following sections.

## 3.3. Characteristics of $C_i^I \Rightarrow C_i^{II} \rightarrow T_k^I$ twinning

Fig. 3a is an EBSD map showing  $\{11\overline{2}2\} \Rightarrow \{11\overline{2}4\} \rightarrow \{10\overline{1}2\}$  or  $C_i^I \Rightarrow C_j^{II} \rightarrow T_k^I$  twins. Two regions marked by white boxes are magnified in Fig. 3b and c. Using the same method in Section 2.3, twin variants are determined with the aid of the pole figures of  $\{11\overline{2}4\}$  planes,  $\{11\overline{2}2\}$  planes and  $\{10\overline{1}2\}$  planes, respectively. Taking twin structure in Fig. 3b as example, the pole figures of  $\{11\overline{2}4\}$  planes (Fig. 3e),  $\{11\overline{2}2\}$  planes (Fig. 3f) and  $\{10\overline{1}2\}$  planes (Fig. 3g) enable us to determine the three variants  $C_6^I$ ,  $C_3^I$  and  $T_4^I$  as denoted

in Fig. 3b. Fig. 3c shows two  $\{10\overline{1}2\}$  twin variants. The corresponding pole figures in Fig. 3g and h determine them to be  $T_4^l$  and  $T_3^l$ , respectively. Therefore, the crystallographic relation is described as  $C_3^l \Rightarrow C_1^l \ominus T_3^l$  or  $T_4^l$ . As depicted in Fig. 3d, the twins  $C_3^l$  and  $C_6^l$  are the co-zone twin. The zone axes of the  $C_3^l$  (yellow) and  $C_6^l$  twins (pink) are parallel but along the opposite directions. The zone axes of the stimulated  $T_4^l$  and  $T_3^l$  twins are indicated by the dashed red lines. It can be seen that the zone axis of the  $C_3^l$  is the sum of the zone axes of the  $T_3^l$  and  $T_4^l$  twins (highlighted in blue). More importantly, twinning shear associated with  $T_3^l$  and  $T_4^l$  twins is mirror symmetry about the shear plane of  $C_3^l$  twin. Thus,  $T_3^l$  and  $T_4^l$  twins are equivalent with respect to the resulted shear on the shear plane of  $C_3^l$  twin.

We identified 28 {11 $\overline{2}4$ } and {11 $\overline{2}2$ } twin-twin junctions and 16 {10 $\overline{1}2$ } twins. All of them can be described as  $C_i^l \Rightarrow C_{i+3}^{ll} \rightarrow T_i^l$  and  $T_{i+1}^{l}$ . It is noticed that  $C_i^l$  and  $C_{i+3}^{ll}$  twins are co-zone twin.  $T_i^l$  and  $T_{i+1}^{l}$  twins are equivalent with respect to the resulted shear on the shear plane of  $C_i^l$  twin. These crystallographic characters will be used to discuss the apparent prevalence of secondary twin variants.

#### 4. Sequential twinning mechanisms

Twin nucleation is driven by local stresses and deformation gradient [54]. For secondary/sequential twinning, several criteria including apparent Schmid factor (a-SF) [27], displacement gradient accommodation (DGA) [55], modified-DGA [45] and nucleation based on dislocation dissociation (NDD) [45,56] have been proposed to address the selection of twin variants observed in experiments [27,43,56,57]. Under shock loading, local stresses are too complex to solely make use of apparent Schmid factor for predicting preferred variants of sequential twins. The other three criteria were proposed based on the accommodation to a local

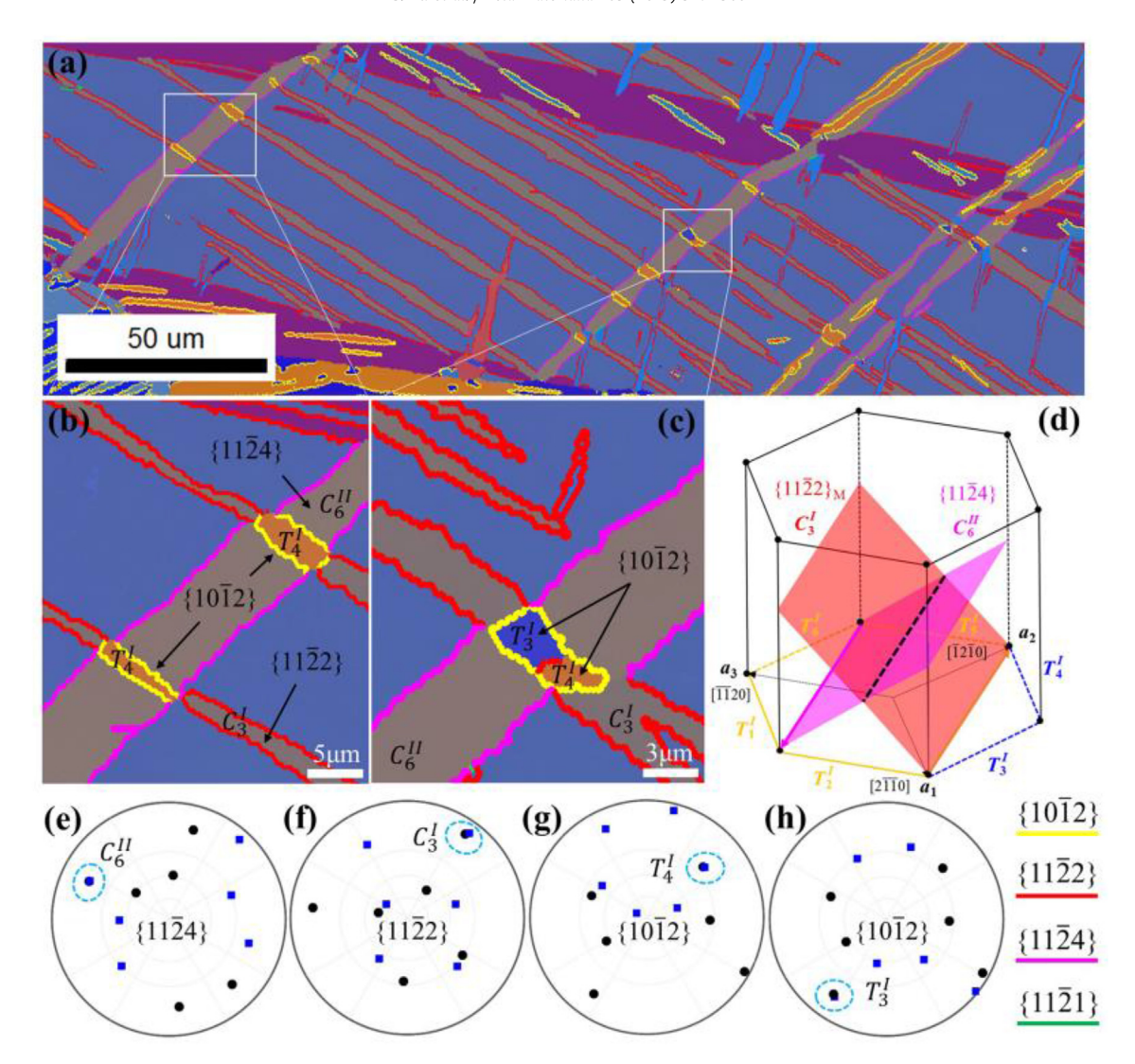


Fig. 3. (a) EBSD characterization of  $\{11\overline{2}4\}$  twin-twin junctions, showing  $\{10\overline{1}2\}$  secondary twins in the junctions. (b) and (c) The magnified EBSD maps of the twin configurations labelled in (a). (d) The crystallography of  $C_6^{ll}$   $C_3^l$ ,  $T_3^l$  and  $T_4^l$  twins. The pole figures of (e)  $\{11\overline{2}4\}$  twinning planes, (f)  $\{11\overline{2}2\}$  twinning planes, (g-h)  $\{10\overline{1}2\}$  twinning planes. The black dots and blue squares represent the parent and twin, respectively. (For interpretation of the references to color in this figure legend, the reader is referred to the Web version of this article.)

twinning shear with focus on either maximizing the deformation gradient accommodation or minimizing the resulted deformation gradient in the vicinity of the local shear. Corresponding to the two observed sequential twinning processes, new twins are more likely associated with shear transformation. Displacement gradient accommodation (DGA) criterion is thus firstly employed to examine proposed sequential twinning mechanisms.

## 4.1. $T_i^{II} \Rightarrow P \rightarrow T_i^I$ twinning

 $\{10\overline{1}2\}$  twin  $(T_j^I)$  with the Burgers vector  $\boldsymbol{b}_{tw}^{\{10\overline{1}2\}} = \frac{3a^2-c^2}{3a^2+c^2}[\overline{1}011]$  and a small shear strain of 0.175 (c/a=1.587) [58] are easily activated in hexagonal metals without dependence on strain rate.  $\{11\overline{2}1\}$  twin  $(T_i^{II})$  with the Burgers vector  $\boldsymbol{b}_{tw}^{\{11\overline{2}1\}} = \frac{a^2}{3a^2+12c^2}[\overline{11}26]$  and a large strain value of 0.63 are often observed at high strain rate in  $\alpha$ -titanium [16,25]. Along with twin propagation and growth, TDs may pile up by conquering repulsive force among successive TDs to form steps or even facets. Shock loading is thus in favour of the formation of steps because of the high strain rate and corresponding high shear stress. These steps associated with TDs pileup

can be treated as a glide-disclination that is associated with the locally high stress/strain concentrations [59]. Under high strain rate, these steps may act as sources for nucleating dislocations, twins, or other shear carriers. For example, twin-twin interaction induced amorphization is reported in FeCoCrNi high-entropy alloy subjected to high-pressure torsion [60]. Phase transformation was stimulated by the twin-twin interaction, such as  $\varepsilon$  martensite in nanostructured bainite under high-strain rate deformation [61] and  $\alpha$ ' martensite in Fe-15Mn-0.6C-2Cr-xN under tension [62].

Fig. 4a shows a schematic model where sequential twins nucleate at steps along {11 $\overline{2}$ 1} twin. Fig. 4b shows atomic structure of a sharp basal || basal step along the (11 $\overline{2}$ 1) twinning plane ( $T_3^{II}$ ). An 80  $\times$  80  $\times$  1.53 nm bi-crystal model is created according to (11 $\overline{2}$ 1) twin orientation. The coordinate is x-axis along the twin shear  $\eta = [\overline{11}26]$ , y-axis along the normal of (11 $\overline{2}$ 1) plane and z-axis along the zone axis [ $\overline{1}$ 100]. With the application of Barnett-Lothe solutions [63] for the displacement field of dislocations in the bi-crystal, 20 TD dipoles under current coordinate are successively introduced into matrix with 10 nm distance. With a fixed boundary condition in x- and y-direction and periodic boundary

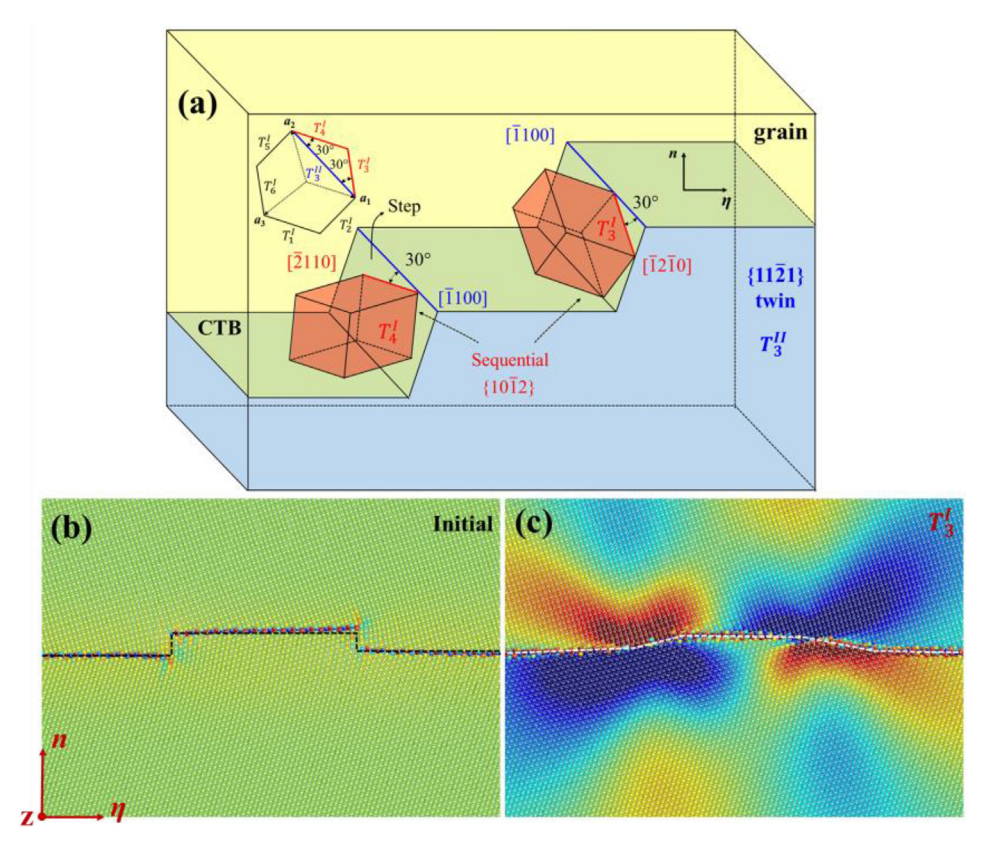


Fig. 4. (a) A schematic of  $T_i^I \Rightarrow P \rightarrow T_j^I$  twinning mechanisms, showing the formation of  $T_3^I$  and  $T_4^I$  {10 $\overline{1}$ 2} sequential twins at the step along the  $T_3^I$  {11 $\overline{2}$ 1} twin boundary. (b) Atomic structure of sharp basal || basal steps along {11 $\overline{2}$ 1} twin boundary. (c) Atomic structure of relaxed steps, showing the local stress field associated with  $T_3^I$  twinning.  $\mathbf{n}$  is the normal of  $T_3^I$  twinning plane,  $\eta$  is the twin shear direction, and z is the zone axis of  $T_3^I$  twin.

condition in z-direction, the model in Fig. 4b is relaxed at 1 K and two steps degenerate into an array of TDs. The shear stress associated with  $T_3^l$  twinning is then plotted in Fig. 4c. It is noted that positive shear stress happens near the left step, implying the twinning process  $T_3^l \Rightarrow P \rightarrow T_3^l$  only occurs at the left step.

According to the EBSD results,  $T_i^I$  and  $T_{i+1}^I$  twins are preferred at  $T_i^{II}$  TB. As depicted in Fig. 4a, the traces of  $T_3^{II}$ ,  $T_3^{I}$  and  $T_4^{I}$  twinning planes interact with the basal plane along  $[\overline{1}100]$  (blue line),  $[\overline{1}2\overline{1}0]$ (red line) and  $[\overline{2}110]$  directions (red line), respectively. The blue vector is the sum of the two red vectors, as shown in the hexagon in the upper left corner of Fig. 4a. Corresponding to the nucleation mechanism for sequential twins at steps along  $\{11\overline{2}1\}$ , the preferred variant of sequential twins  $\{10\overline{1}2\}$   $(T_i^l)$  should maximize the accommodation to the deformation gradient created by  $\{11\overline{2}1\}$   $(T_i^{II})$ twin. We thus transform the deformation gradient created by  $\{11\overline{2}1\}(T_i^{II})$  twin into the sequential twinning reference frame of six potential  $\{10\overline{1}2\}$  twins. The results are listed in Table 2. The bigger the component  $e_{13}$  is, the better accommodation ability the twin variant has. The results clearly show an order in terms of the accommodation ability of six potential  $\{10\overline{1}2\}$  twins to the local shear caused by the  $T_i^{II}$  twin, i.e.,  $T_{i}^{II} \Rightarrow P \rightarrow T_i^{I}$  and  $T_{i+1}^{I} > T_i^{II} \Rightarrow P \rightarrow T_{i+2}^{I}$  and  $T_{i+5}^{II} > T_i^{II} \Rightarrow P \rightarrow T_{i+3}^{I}$  and  $T_{i+4}^{I}$ . The result is in good agreement with the experimental observation.

## 4.2. $C_{i}^{I} \Rightarrow C_{i+3}^{II} \rightarrow T_{k}^{I}$ twinning

 $C_i^I \Rightarrow C_{i+3}^{II} \to T_k^I$  twinning describes the interaction process of the  $C_i^I$  twin with the  $C_{i+3}^{II}$  twin, leading to the formation of secondary

twins  $T_k^I$  inside the  $C_{i+3}^{II}$  twin. Twin-twin interactions in hexagonal metals have been studied by Robert Reed-Hill et al. since 1960's [64]. Recently, Yu et al. [28,40] systematically investigated the interactions between two of  $\{10\overline{1}2\}$  twin variants in Mg based on their EBSD observations and crystallographic models. Twin transmission rarely happens because only available twinning mode  $\{10\overline{1}2\}$  is difficult to be activated in the same mode twin under monotonic loading. Instead, a basal slip band is resulted in the vicinity of the contact site [40]. Gong et al. [65] conducted atomistic simulations of non-cozone twin—twin interactions in Mg and accounted for the structural characters of twin-twin junctions based on the local stresses associated with twin-twin interactions.

Unlike one primary twinning in Mg, there are more available twinning modes in Ti. Twin-twin interactions in Ti may cause sequential twins that are in different twinning modes from the primary twins. Fig. 5 illustrates the interaction of the  $C_i^l$  twin with the  $C_{i+3}^{ll}$  twin. The two twins  $C_i^l$  and  $C_{i+3}^{ll}$  are co-zone, sharing the same zone axis along [ $\overline{1}010$ ] (blue line). As the incoming twin  $C_i^l$  interacts the primary twin  $C_{i+3}^{ll}$ , stimulating secondary  $\{10\overline{1}2\}$  twins at the intersection region inside the  $C_{i+3}^{ll}$  twin. Corresponding to the m-DGA criterion, the preferred variant of sequential twins  $\{10\overline{1}2\}$  ( $T_k^l$ ) in the  $C_{i+3}^{ll}$  twin should be able to maximize the accommodation to the deformation gradient associated with the incoming  $C_i^l$  twin. We thus transform the deformation gradient created by the  $C_i^l$  twin into the sequential twinning reference frame of six  $T_k^l$  twins in the  $C_{i+3}^{ll}$  twin. The results are listed in Table 2. The order of the accommodation ability associated with the sequential  $\{10\overline{1}2\}$  twin variants to the deformation gradient created by the  $C_i^l$  twin variants to the deformation gradient created by the  $C_i^l$  twin variants to the deformation gradient created by the  $C_i^l$  twin variants to the deformation gradient created by the  $C_i^l$  twin is  $C_i^l \Rightarrow C_{i+3}^{ll} \to T_i^l$  and  $T_{i+1}^l$  (Type A)  $> C_i^l \Rightarrow C_{i+3}^{ll} \to T_{i+2}^l$  and  $T_{i+5}^l$  (Type B)  $> C_i^l \Rightarrow C_{i+3}^{ll} \to T_{i+3}^l$  and  $T_{i+4}^l$  (Type C). It is worth pointing

**Table 2** Expression of the displacement gradient tensor associated with the  $(11\overline{2}1)(<\overline{11}26)>$  twin into the twinning reference frame of the six potential  $\{10\overline{1}2\}$  twin variants in the same grain. Expression of the displacement gradient tensor associated with the  $(11\overline{2}1)(<11\overline{2}3)>$  twin into the twinning reference frame of the six potential  $\{10\overline{1}2\}$  and six  $\{11\overline{2}1\}$  twin variants inside the  $(\overline{11}24)<\overline{22}4\overline{3}>$  twin.

$(11\overline{2}1) \Rightarrow P \rightarrow \{10\overline{1}2\}$	m-DGA	(11 <del>2</del> 2)⇒( <del>11</del> 24) →{10 <del>1</del> 2}	m-DGA	$(11\overline{2}2) \Rightarrow (\overline{11}24)$ $\rightarrow \{11\overline{2}1\}$	m-DGA
$(10\overline{1}2)[\overline{1}011]$ $T_i^{II} \Rightarrow P \rightarrow T_i^{I}$	$\begin{bmatrix} -0.21 & -0.25 & 0.41 \\ -0.04 & -0.05 & 0.07 \\ -0.14 & -0.16 & 0.26 \end{bmatrix}$	$(10\overline{1}2)[\overline{1}011]$ $C_i^I \Rightarrow C_{i+3}^{II} \rightarrow T_i^I$	$\begin{bmatrix} 0 & -0.07 & 0.19 \\ 0 & -0.03 & 0.07 \\ 0 & -0.01 & 0.02 \end{bmatrix}$	$(11\overline{2}1)[\overline{11}26]$ $C_i^I \Rightarrow C_{i+3}^{II} \rightarrow T_i^{II}$	$\begin{bmatrix} 0.09 & 0 & 0.17 \\ 0 & 0 & 0 \\ -0.05 & 0 & -0.09 \end{bmatrix}$
$(01\overline{1}2)[0\overline{1}11]$ $T_i^{II} \Rightarrow P \rightarrow T_{i+1}^{I}$	$\begin{bmatrix} -0.21 & 0.25 & 0.41 \\ 0.04 & -0.05 & -0.07 \\ -0.14 & 0.16 & 0.26 \end{bmatrix}$	$(01\overline{1}2)[0\overline{1}11]$ $C_{i}^{I} \Rightarrow C_{i+3}^{II} \rightarrow T_{i+1}^{I}$	$\begin{bmatrix} 0 & 0.07 & 0.19 \\ 0 & -0.03 & -0.07 \\ 0 & 0.01 & 0.02 \end{bmatrix}$	$(\overline{1211})[1\overline{2}16]$ $C_i^I \Rightarrow C_{i+3}^{II} \rightarrow T_{i+1}^{II}$	$\begin{bmatrix} 0.10 & 0.11 & 0.10 \\ -0.08 & -0.08 & -0.07 \\ -0.02 & -0.02 & -0.02 \end{bmatrix}$
$(\overline{1}102)[1\overline{1}01]$ $T_i^{II} \Rightarrow P \rightarrow T_{i+2}^{I}$	$\begin{bmatrix} 0.08 & 0.39 & 0.09 \\ -0.04 & -0.18 & -0.04 \\ 0.09 & 0.42 & 0.10 \end{bmatrix}$	$(\overline{1}102)[1\overline{1}01]$ $C_i^I \Rightarrow C_{i+3}^{II} \to T_{i+2}^I$	$\begin{bmatrix} 0.05 & -0.08 & 0.06 \\ 0.07 & -0.11 & 0.09 \\ 0.06 & -0.08 & 0.06 \end{bmatrix}$	$(\overline{2}111)[2\overline{11}6]$ $C_i^I \Rightarrow C_{i+3}^{II} \rightarrow T_{i+2}^{II}$	$\begin{bmatrix} 0.10 & -0.11 & 0.10 \\ 0.08 & -0.08 & 0.07 \\ -0.02 & 0.02 & -0.02 \end{bmatrix}$
$(\overline{1}012)[10\overline{1}1]$ $T_i^{II} \Rightarrow P \rightarrow T_{i+3}^{I}$	$\begin{bmatrix} 0.23 & 0.14 & -0.10 \\ -0.08 & -0.05 & 0.03 \\ 0.45 & 0.26 & -0.19 \end{bmatrix}$	$(\overline{1}012)[10\overline{1}1]$ $C_i^I \Rightarrow C_{i+3}^{II} \rightarrow T_{i+3}^I$	$\begin{bmatrix} 0.01 & 0 & 0 \\ -0.07 & -0.03 & -0.01 \\ 0.19 & 0.07 & 0.02 \end{bmatrix}$	$(\overline{1121})[11\overline{2}6]$ $C_i^I \Rightarrow C_{i+3}^{II} \rightarrow T_{i+3}^{II}$	$\begin{bmatrix} 0.09 & 0 & -0.05 \\ 0 & 0 & 0 \\ 0.17 & 0 & -0.09 \end{bmatrix}$
$(0\overline{1}12)[01\overline{1}1]$ $T_i^{II} \Rightarrow P \rightarrow T_{i+4}^{I}$	$\begin{bmatrix} 0.23 & -0.14 & -0.10 \\ 0.08 & -0.05 & -0.03 \\ 0.45 & -0.26 & -0.19 \end{bmatrix}$	$(0\overline{1}12)[01\overline{1}1]$ $C_i^I \Rightarrow C_{i+3}^{II} \rightarrow T_{i+4}^I$	$\begin{bmatrix} 0.01 & 0 & 0 \\ 0.07 & -0.03 & 0.01 \\ 0.19 & -0.07 & 0.02 \end{bmatrix}$	$(1\overline{2}11)[\overline{1}2\overline{1}6]$ $C_i^I \Rightarrow C_{i+3}^{II} \to T_{i+4}^{II}$	$\begin{bmatrix} 0.10 & -0.08 & -0.02 \\ 0.10 & -0.08 & -0.02 \\ 0.09 & -0.07 & -0.02 \end{bmatrix}$
$(1\overline{1}02)[\overline{1}101]$ $T_i^{II} \Rightarrow P \rightarrow T_{i+5}^{I}$	$\begin{bmatrix} 0.08 & -0.39 & 0.09 \\ 0.04 & -0.18 & 0.04 \\ 0.09 & -0.42 & 0.10 \end{bmatrix}$	$(1\overline{1}02)[\overline{1}101]$ $C_i^I \Rightarrow C_{i+3}^{II} \rightarrow T_{i+5}^I$	$\begin{bmatrix} 0.05 & 0.08 & 0.06 \\ -0.07 & -0.11 & -0.08 \\ 0.06 & 0.08 & 0.06 \end{bmatrix}$	$(2\overline{11}1)[\overline{2}116]$ $C_i^I \Rightarrow C_{i+3}^{II} \rightarrow T_{i+5}^{II}$	$\begin{bmatrix} 0.10 & 0.08 & -0.02 \\ -0.10 & -0.08 & 0.02 \\ 0.09 & 0.07 & -0.02 \end{bmatrix}$

out that the accommodation ability via  $T_i^l$  or  $T_{i+1}^l$  is equivalent because their shear is mirror symmetry about the shear plane of the incoming twin. Thus, the nucleation of both or one of  $T_i^l$  and  $T_{i+1}^l$  is arbitrary. These phenomena are exactly observed in our experiments, one variant in Fig. 3b and two variants in Fig. 3c.

#### 5. Discussion

The experiment phenomena are so far well accounted for by our proposed sequential twinning mechanisms. Here, we further discuss the feasibility of these twinning mechanisms based on dislocation theory and local stress fields.

# 5.1. Emissary twinning disconnections in association with $T_i^{II} \Rightarrow P \rightarrow T_i^{I}$ twinning

The steps along the twin boundaries may act as the source for nucleating other twins via emissary twinning disconnections. When TDs associated with  $(11\overline{2}1)$  ( $T_l^{II}$ ) twinning pile up at the steps along the twin boundaries, these TDs may dissociate into TDs associated with  $\{10\overline{1}2\}$  twinning. One twinning dislocation of the  $T_l^{II}$  twin,  $b_t^{(11\overline{2}1)}$ , can dissociate into x twining dislocations  $xb_t^{(1012)}$ 

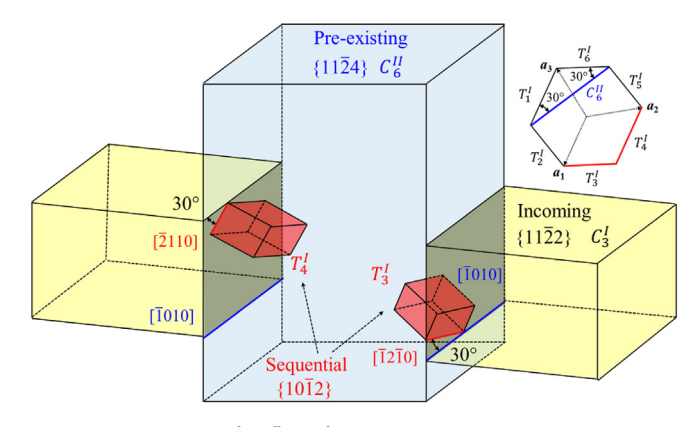


**Fig. 5.** (a) A schematic of  $C_i^l \Rightarrow C_{i+3}^l \rightarrow T_k^l$  twinning mechanisms, showing the interaction of incoming  $\{11\overline{2}2\}$  twin  $C_3^l$  and pre-existing  $\{11\overline{2}4\}$  twin  $C_6^l$  and the activation of  $\{10\overline{1}2\}$  twins  $T_3^l$  and  $T_4^l$  inside  $C_6^l$ .

and a residual dislocation  $b_r^m$ , where the superscript m represents the mth  $(m=1 \dots 6)$   $\{10\overline{1}2\}$  twin variant. The results are listed in Table 3. When x=1, the elastic energy of these dislocations is reduced for  $T_i^I$  and  $T_{i+1}^I$  twin variants according to the Frank's law, while the elastic energy of the dislocations corresponding to the dissociation into other four  $\{10\overline{1}2\}$  twins increases. The results clearly indicate that  $T_i^{II} \Rightarrow P \rightarrow T_i^I$  or  $T_{i+1}^I$  should dominate among the six possibilities. This coincides with the results from EBSD characterization.

We further calculate the local stress field associated with the pileup of  $b_t^{(1121)}$  TDs by using a CP-FFT approach with the Düsseldorf Advanced Material Simulation Kit (DAMASK) [66]. Fig. 6a shows a bi-crystal simulation cell. The lower crystal is  $(11\overline{2}1)$  twin  $(T_3^{II})$  and the upper crystal is the matrix. If a thin twin grows into the matrix, two steps form associated with the pileup of  $b_t^{(11\overline{2}1)}$  TDs. Without the loss of the generality, the two steps are 45° inclined to the twinning plane. The simulation cell adopts the coordinate, xaxis along  $[1\overline{1}00]$ , y-axis along the normal of  $(11\overline{2}1)$  plane and zaxis along  $[\overline{11}26]$  in the matrix. The model is discretized by a regular grid of  $2 \times 354 \times 512$  voxels. Phenomenological law was used to describe dislocation slip (see Appendix A). Basal <a>, prismatic  $\langle a \rangle$  and pyramidal  $\{10\overline{1}1\} \langle c+a \rangle$  dislocation slips are considered and their critical resolved shear stresses (CRSS) are 141 MPa, 254 MPa and 338 MPa, respectively [67]. The corresponding twinning shear  $\gamma_{\nu z} = 0.63$  is applied to the newly formed twin domain in 10 increments. The finite strain spectral method implemented in DAMASK is used to solve the stress fields due to the Eigenstrain  $\gamma_{vz}$ in the newly formed twin domain [66]. In order to exploit the effect of strain rate on the local stress field, we simulate the newly formed twin with various growth rates,  $0.63 \times 10^2$ /s, 0.63/s and  $0.63 \times 10^2$  $10^{-4}$ /s. To interpret the stress field around the steps and infer the driving force for further  $\{10\overline{1}2\}$  twinning, the resolved shear stress (RSS) associated with the six  $\{10\overline{1}2\}$  twin variants are calculated and compared.

Due to the mirror symmetry between  $T_1^I$  and  $T_6^I$ ,  $T_2^I$  and  $T_5^I$ ,  $T_3^I$  and  $T_4^I$  with respect to the shear plane of (11 $\overline{2}$ 1) twin, RSS associated with  $T_2^I$ ,  $T_4^I$  and  $T_6^I$  is compared. The RSS associated with  $T_4^I$  at a growth strain rate of 0.63/s is shown in Fig. 6b. The RSS is positive in the matrix around the left step, while negative in the matrix around the right step. The shear direction of the (11 $\overline{2}$ 1) twin is along the positive x direction. This implies that the activation of  $\{10\overline{1}2\}$  twin

**Table 3** The residual dislocation and the elastic energy associated with the dislocation dissociation for  $(11\overline{2}1) \Rightarrow P \rightarrow \{10\overline{1}2\}$  and  $(11\overline{2}2) \Rightarrow (\overline{11}24) \rightarrow \{10\overline{1}2\}$ .

$(11\overline{2}1) \Rightarrow P \rightarrow \{10\overline{1}2\}$	х	$b_r^m$	$ b_i ^2$	$\left b_r^m\right ^2$	$x b_t ^2$
(1012)[1011]	1	[0.06 0.030.030.09]	0.79	0.26	0.36
$T_i^{II} \Rightarrow P \rightarrow T_i^{I}$					
$(01\overline{1}2)[0\overline{1}11]$	1	$[\overline{0.03} \ 0.06 \ \overline{0.03} 0.09]$	0.79	0.26	0.36
$T_i^{II} \Rightarrow P \rightarrow T_{i+1}^{I}$					
$(\overline{1}102)[1\overline{1}01]$	1	$[\overline{0.12} \ 0.06 \ 0.06 \ 0.09]$	0.79	0.46	0.36
$T_i^{II} \Rightarrow P \rightarrow T_{i+2}^{I}$					
$(\overline{1}012)[10\overline{1}1]$	1	$[\overline{0.12} \ \overline{0.03}0.15 \ 0.09]$	0.79	0.46	0.36
$T_i^{II} \Rightarrow P \rightarrow T_{i+3}^{I}$					
$(0\overline{1}12)[01\overline{1}1]$	1	$[\overline{0.03} \ \overline{0.12}0.15 \ 0.09]$	0.79	0.46	0.36
$T_i^{II} \Rightarrow P \rightarrow T_{i+4}^I$					
$(1\overline{1}02)[\overline{1}101]$	1	$[0.06 \ \overline{0.12}0.06 \ 0.09]$	0.79	0.46	0.36
$T_i^{II} \Rightarrow P \rightarrow T_{i+5}^I$					
$(11\overline{2}2) \Rightarrow (\overline{11}24) \rightarrow \{10\overline{1}2\}$	X	$b_r^m$	$ b_i ^2$	$ b_r^m ^2$	$x b_t ^2$
$(10\overline{1}2)[\overline{1}011]$	1	$[\overline{0.02} \ 0.07 \ \overline{0.05} 0.04]$	0.67	0.12	0.36
$C_i^I \Rightarrow C_{i+3}^{II} \rightarrow T_i^I$					
$(01\overline{1}2)[0\overline{1}11]$	1	$[0.07 \ \overline{0.020.05}0.04]$	0.67	0.12	0.36
$C_i^I \Rightarrow C_{i+3}^{II} \rightarrow T_{i+1}^I$					
$(\overline{1}102)[1\overline{1}01]$	1	$[\overline{0.02} \ 0.15 \ \overline{0.13} \ 0.04]$	0.67	0.56	0.36
$C_i^I \Rightarrow C_{i+3}^{II} \rightarrow T_{i+2}^I$					
$(\overline{1}012)[10\overline{1}1]$	1	$[0.15 \ 0.07 \ \overline{0.22}0.04]$	0.67	1.00	0.36
$C_i^I \Rightarrow C_{i+3}^{II} \rightarrow T_{i+3}^I$					
$(0\overline{1}12)[01\overline{1}1]$	1	$[0.07 \ 0.15 \ \overline{0.22}0.04]$	0.67	1.00	0.36
$C_i^I \Rightarrow C_{i+3}^{II} \rightarrow T_{i+4}^I$					
$(1\overline{1}02)[\overline{1}101]$	1	$[0.15 \ \overline{0.020.13}0.04]$	0.67	0.56	0.36
$C_i^I \Rightarrow C_{i+3}^{II} \rightarrow T_{i+5}^I$					

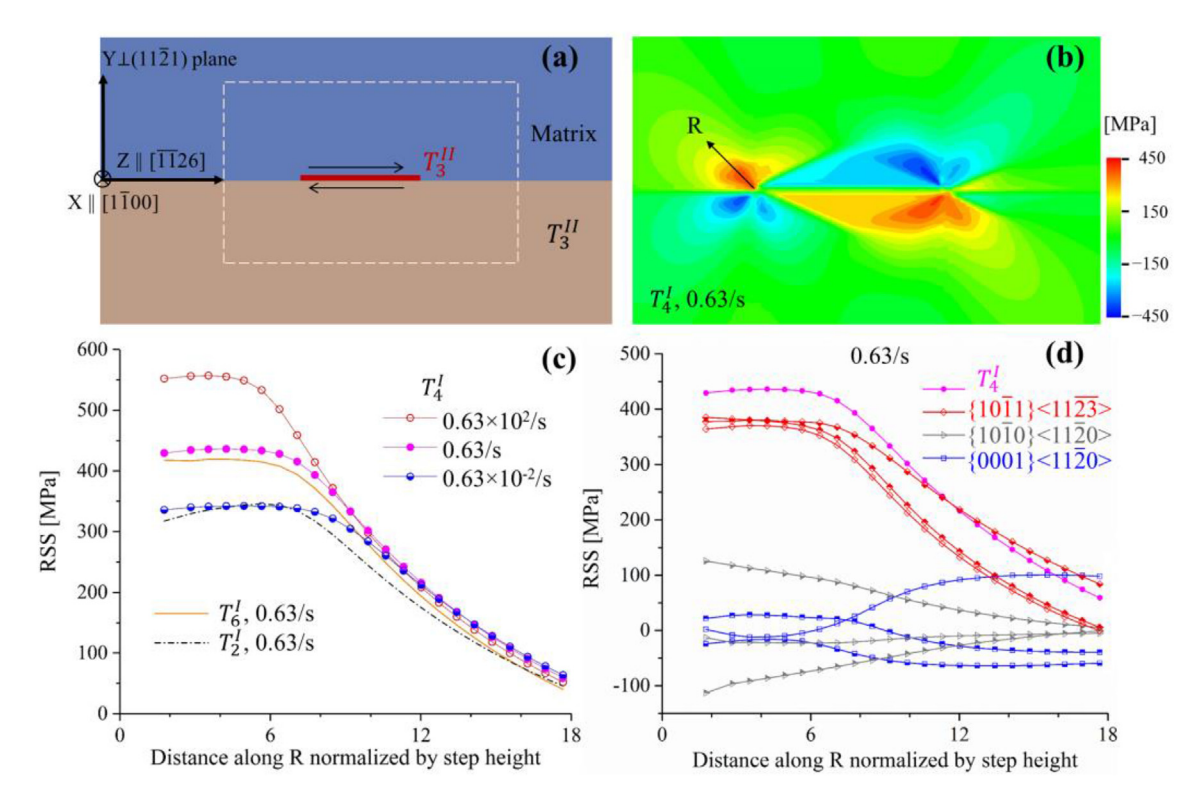


**Fig. 6.** (a) Bi-crystal unit cell used in CP-FFT to calculate the local stress field associated with the formation of  $45^{\circ}$  inclined steps along coherent twin boundary of twin  $T_3^{II}$ . The red band represents newly formed twin  $T_4^{II}$ . A twinning shear  $\gamma_{yz} = 0.63$  is applied in the red band. (b) The resolved shear stress field associated with  $T_4^{II}$  twinning as twin  $T_3^{II}$  forms at a growth rate of 0.63/s. (c) Variation of RSSes associated with  $T_4^{II}$  along the vector R in (b) at three growth rates of the step. (d) Comparison of RSSes associated with  $T_4^{II}$  (pink), pyramidal  $\langle c\mathbf{r}+\mathbf{a}\rangle$  dislocations (red), prismatic  $\langle \mathbf{a}\rangle$  dislocation (black) and basal  $\langle \mathbf{a}\rangle$  dislocations (blue) as twin  $T_3^{II}$  forms at a growth rate of 0.63/s. (For interpretation of the references to color in this figure legend, the reader is referred to the Web version of this article.)

just occurs at the step which moves along the opposite direction of the twin shear. Thus, the twin plane of newly activated twins has an obtuse angle with respect to the twin shear of the  $(11\overline{2}1)$  twin, which is consistent with experimental observations as revealed in Section 2.3. We compare RSSes of TDs associated with  $T_2^l$ ,  $T_4^l$  and  $T_6^l$  at the growth rate of 0.63/s,  $T_4^l$  twinning shall be favorable than others because of the highest RSS (Fig. 6c). In addition, the RSS associated with  $T_4^l$  twinning increases (Fig. 6c) with increasing the growth rate, implying that high strain rate will facilitate the activation of sequential twining. This is attributed to incompletely plastic relaxation associated with dislocation slips. Fig. 6d shows RSSes of various dislocations at the strain rate of 0.63/s. It is found that the RSS associated with pyramidal  $\langle <\mathbf{c}+\mathbf{a} \rangle >$  dislocations near the step are still higher than the CRSS.

# 5.2. Shear transformation in association with $C_i^I \Rightarrow C_{i+3}^{II} \rightarrow T_k^I$ twinning

When the propagation of  $\{11\overline{2}2\}$  ( $C_i^I$ ) twins is blocked by a  $\{11\overline{2}4\}$   $(C_{i+3}^{II})$  twin, the localized twinning shear could transform into the  $\{11\overline{2}4\}$  ( $C_{i+3}^{II}$ ) twin via sequential  $\{10\overline{1}2\}$  twinning. We analyze the nucleation and emission of twinning disconnections associated with six  $\{10\overline{1}2\}$  secondary twins  $(T_i^I)$  inside the  $(\overline{11}24)$ twin  $(C_6^{II})$ . The incoming twinning disconnection associated with the (11 $\overline{2}$ 2) twin ( $C_3^I$ ) has the Burgers vector,  $\boldsymbol{b}_{tw}^{\{11}$  $\overline{2}$ 2 $\}$  $\frac{c^2-2a^2}{3(c^2+a^2)}$  [11 $\overline{23}$ ] [9]. The dislocation line of the  $C_3^l$  TDs on the  $C_6^{ll}$  twin boundary aligns along [1 $\overline{100}$ ]. For  $T_3^l$  and  $T_4^l$  twins, their intersection line with the  $C_6^{II}$  twin boundary is along  $\langle <10\ \overline{14}\ 4\ 3\rangle >$ , which has a 20.2° misalignment angle with the incoming dislocation line. For  $T_2^l$  and  $T_5^l$  twins, their intersection line with the  $C_6^{ll}$ twin boundary is along  $\langle <1\overline{5}43\rangle >$ , which has a misalignment angle of 55.8° with the incoming dislocation line. For  $T_1^I$  and  $T_6^I$  twins, their intersection line with the  $C_6^{II}$  twin boundary is along  $\langle <22\overline{4}3\rangle$ >, which is perpendicular to the incoming dislocation line. It has been widely recognized that the smallest misalignment is the easiest pathway for slip transformation. This analysis gives a clear tendency to produce twinning dislocations associated with six {1012} twins within the  $C_6^{II}$  twin, i.e.,  $C_3^I \Rightarrow C_6^{II} \rightarrow T_3^I$  and  $T_4^I > C_3^I \Rightarrow$  $C_6^{II} \rightarrow T_2^I$  and  $T_5^I > C_3^I \Rightarrow C_6^{II} \rightarrow T_1^I$  and  $T_6^I$ . This trend is consistent with our experimental observation and the analysis based on deformation gradient accommodation.

Accompanying slip transformation via nucleation and emission of twinning disconnections inside  $C^{II}_{i+3}$  twin, the residual dislocations left at the twin-twin boundary and the change in elastic energy of dislocations are summarized in Table 3. A twinning dislocation associated with the  $C^{I}_{3}$  twin,  $b^{\{10\overline{12}\}}_{1}$ , can be dissociated into one secondary twining dislocations  $b^{\{10\overline{12}\}}_{t}$  inside the  $C^{II}_{6}$  twin and a residual dislocation  $b^{m}_{r}$ . The results reveal that the dislocation dissociation of  $C^{I}_{3}$  twin only favorably produces twinning dislocation associated with  $T^{I}_{3}$  and  $T^{I}_{4}$  secondary twins inside the  $C^{II}_{6}$  twin. The other dissociations corresponding to  $T^{I}_{1}$ ,  $T^{I}_{2}$  and  $T^{I}_{5}$  and  $T^{I}_{6}$  secondary twins inside the  $C^{II}_{6}$  twin are accompanied with an increase in the elastic energy of dislocations. In the other words,  $C^{I}_{i} \Rightarrow C^{II}_{i+3} \rightarrow T^{I}_{i}$  or  $T^{I}_{i+1}$  should be predominant among six possibilities. This agrees well with the experimental observations.

We also calculate the local stress field associated with the pileup of  $b_t^{(11\overline{2}2)}$  TDs blocked at the  $(\overline{11}24)$  twin boundaries using DAM-ASK. The model is shown in Fig. 7a and the unit cell is discretized by a regular grid of  $2\times240\times480$  voxels. An isotropic soft-elastic buffer layer is adopted to simulate the free boundary conditions,

similar to the methods in Ref. [66]. Parameters of constitutive law describing dislocation slip are listed in Appendix A. The corresponding twinning shear  $\gamma_{yz}=0.218$  is applied to the (11 $\overline{2}2$ ) twin region in 10 increments. The stress fields due to the Eigenstrain  $\gamma_{yz}$  is solved in DAMASK [66]. The local stress fields are calculated at strain rates of 0.218  $\times$  10 $^{-2}$ /s, 0.218/s and 0.218  $\times$  10 $^{2}$ /s to study the strain rate effects on the stress fields.

## 5.3. Other issues related to $C_i^I \Rightarrow C_{i+3}^{II} \rightarrow T_k^I$ twinning

Another tension twinning  $\{11\overline{2}1\}$  ( $T_k^{II}$ ) is often activated at high strain rate [25]. However,  $\{11\overline{2}2\} \Rightarrow \{11\overline{2}4\}$  twin-twin interactions don't trigger the formation of  $\{11\overline{2}1\}$  twins. Here we evaluate the accommodation ability of  $\{11\overline{2}1\}$  secondary twins. The deformation gradient created by the  $C_i^I$  twin was transformed into the sequential twinning reference frame of six  $\{11\overline{2}1\}$  twins ( $T_k^{II}$ ) in the  $C_{i+3}^{II}$  twin, as listed in Table 2. The results show that  $T_i^{II}$  is the most effective accommodation variant among six  $\{11\overline{2}1\}$  twins, while it is still less effective than  $T_i^I$  and  $T_{i+1}^I$  (Type A). This trend agrees well with the experimental observation. Once Type A  $\{10\overline{1}2\}$  is activated by  $\{11\overline{2}2\} \Rightarrow \{11\overline{2}4\}$  interaction,  $\{11\overline{2}1\}$  twins don't form.

 $\{11\overline{2}2\} \Rightarrow \{11\overline{2}4\} \rightarrow \{10\overline{1}2\}$  twinning results in  $\{11\overline{2}4\} \rightarrow \{10\overline{1}2\}$  double twins. However, the geometry characters are distinguished from the conventional  $\{11\overline{2}4\} \rightarrow \{10\overline{1}2\}$  double twins. In Ref [45], a statistical observation of  $\{11\overline{2}4\} \rightarrow \{10\overline{1}2\}$  double twins in  $\alpha$ -titanium reveals that only  $C^{II}_{i+3} \rightarrow T^{I}_{i+3}$  or  $T^{I}_{i+4}$  is preferred inside the  $C^{II}_{i+3}$  primary twins, as highlighted in blue in Table 1. The secondary twin variants  $T^{I}_{i+3}$  and  $T^{I}_{i+4}$  can maximally accommodate the strain associated with the  $C^{II}_{i+3}$  primary twins. In this work, the detected  $\{10\overline{1}2\}$  double twins inside  $\{11\overline{2}4\}$  twins are  $C^{II}_{i+3} \rightarrow T^{I}_{i}$  and  $T^{I}_{i+1}$ , which cannot relax the strain associated with the primary  $C^{II}_{i+3}$  twin [45]. Thus,  $\{10\overline{1}2\}$  twinning inside  $\{11\overline{2}4\}$  twins under shock loading is generated for accommodating the strain caused by the incoming  $\{11\overline{2}2\}$  twins rather than the primary  $\{11\overline{2}4\}$  twins.

## 5.4. Does dislocation-TB interaction facilitate $T_i^{II} \Rightarrow P \rightarrow T_j^{I}$ twinning?

Twin boundary blocks dislocations, resulting in the accumulation of high density of dislocations under shock loading. The reaction processes between dislocations and twin boundary could result in many deformation modes, such as reconstruction of twin boundary, sliding and/or migration of twin boundary, deformation twinning in the twin or matrix, and shear/slip bands, etc. [68]. Here

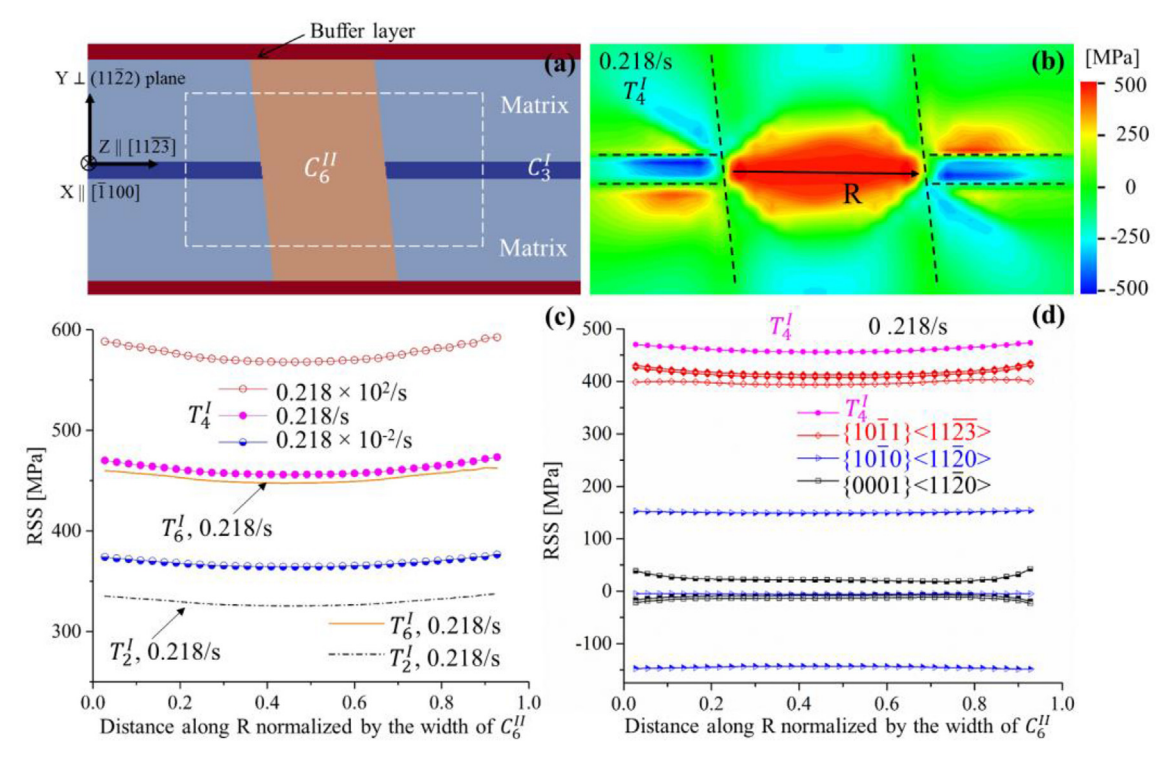


Fig. 7. (a) Unit model used in CP-FFT for calculating the local stress field associated with the interaction of an incoming  $(11\overline{2}2)$  twin  $C_3^l$  with  $(\overline{11}24)$  twin  $C_6^l$ . A twinning shear is applied in  $C_3^l$  ( $11\overline{2}2$ ) twin. (b) RSS associated with  $T_4^l$  as the incoming twin shears at the growth rate of 0.218/s. (c) Variation of RSSes associated with  $T_4^l$  along the R in (b) at three growth rates. (d) Comparison of RSSes associated with  $T_4^l$  twin (pink), pyramidal ( $<\mathbf{c}+\mathbf{a}>$  dislocations (red), prismatic  $<\mathbf{a}>$  dislocation (blue) and basal  $<\mathbf{a}>$  dislocations (black) as the incoming twin shears at the growth rate of 0.218/s. (For interpretation of the references to color in this figure legend, the reader is referred to the Web version of this article.)

we consider the possibility associated with  $T_i^{II} \Rightarrow P \rightarrow T_j^I$  twinning by dislocation-TB interactions.

The intersection lines ( $l_{\rm T}$ ) between the primary (11 $\overline{2}$ 1) and sequential  $\{10\overline{1}2\}$  twin planes align along  $<5\overline{413}>$  for Type A  $(T_3^I)$ and  $T_4^l$ ),  $\langle <5\overline{7}26 \rangle >$  for Type B ( $T_2^l$  and  $T_5^l$ ) and  $\langle <7\overline{8}13 \rangle >$  for Type C  $(T_1^l \text{ and } T_6^l)$ . It is noted that only  $l_T$  for Type A lies in available slip planes, i.e., pyramidal  $\{10\overline{1}1\}$  plane, which provides the geometrical condition for the dissociation of dislocations in the pyramidal slip plane into {1012} twinning (Type A). But dislocation-TB interactions unlikely activate  $\{10\overline{1}2\}$  twinning (Type B and Type C) because of the lack of the geometrical condition. This is consistent with experimental observation, Fig. 8 illustrates slip transformation processes associated with the formation of  $T_3^I$  and  $T_4^I$ . The dissociation process can be described as  $b_{<c+a>} \Rightarrow b_r^m + xb_t^{\{1012\}}$ , where  $b_{<c+a>} = \frac{1}{3} < 11\overline{23} >$ , a = 0.468 nm and c = 0.295 nm for Ti. According to Frank's law, a parameter x is equal to 17 in association with the transformation of the  $(\overline{1}011)$   $[\overline{2}11\overline{3}]$  slips to  $T_3^I$  twin and  $(0\overline{1}11)$   $[1\overline{2}1\overline{3}]$  slips to  $T_4^I$  twin. However, pyramidal slip is often observed at a large strain [69]. Therefore, dislocation-TB interactions may facilitate  $T_i^{ll} \Rightarrow P \rightarrow T_i^{l}$  twinning at low strain rate, but step-facilitated nucleation mechanisms dominate at high strain rate.

## 6. Conclusion

Two types of  $\{10\overline{1}2\}$  sequential twinning processes are for the first time reported according to EBSD characterization of deformed titanium sheets that are subjected to shock loading. One is described as  $\{11\overline{2}1\} \Rightarrow P \rightarrow \{10\overline{1}2\}$   $(T_i^{II} \Rightarrow P \rightarrow T_i^{I})$ , i.e.,  $\{10\overline{1}2\}$ 

sequential twinning is activated in the parent grain (P) along with  $\{11\overline{2}1\}$  twins. The other is described as  $\{11\overline{2}2\} \Rightarrow \{11\overline{2}4\} \rightarrow \{10\overline{1}2\}$   $(C_i^l \Rightarrow C_j^{ll} \rightarrow T_k^l)$ , i.e.,  $\{10\overline{1}2\}$  secondary twinning is stimulated inside  $\{11\overline{2}4\}$  twin by co-zone  $\{11\overline{2}2\}$  twin. A statistical EBSD characterization reveals the well-defined crystallographic relations between sequential  $\{10\overline{1}2\}$  twin variants and the primary twins, i.e.,  $T_i^{ll} \Rightarrow P \rightarrow T_i^{ll}$  or  $T_{i+1}^{ll}$  for the first case and  $C_i^l \Rightarrow C_{i+3}^{ll} \rightarrow T_i^{ll}$  or  $T_{i+1}^{ll}$  for the second case

Regarding  $T_i^{II} \Rightarrow P \rightarrow T_i^I$  or  $T_{i+1}^I$  twinning, we account for the sequential twinning based on emissary twinning disconnections at steps along twin boundary. The steps along the twin boundaries act as the source and stress/strain concentrator for nucleating other twins via emissary twinning disconnections. When TDs associated with  $\{11\overline{2}1\}$   $(T_i^{ll})$  twinning pile up to form a step along the twin boundary, the dissociation of  $T_i^{II}$  TDs can energetically activate  $T_i^I$  or  $T_{i+1}^{\ \ \ \ \ \ \ }$  twin, which agrees with the experiments. The local stress field associated with the pileup of  $b_t^{(11\overline{2}1)}$  TDs is computed by using CP-FFT, showing the highest resolved shear stress associated with the twin variants  $T_i^I$  or  $T_{i+1}^I$  than other variants. Regarding  $C_i^l \Rightarrow C_{i+3}^{ll} \rightarrow T_i^l$  or  $T_{i+1}^l$  twinning, the nucleation of the sequential  $\{10\overline{1}2\}$  twins is accomplished via slip transformation associated with incoming TDs of  $\{11\overline{2}2\}$  twin into the primary  $\{11\overline{2}4\}$  twin. The local stress field associated with the pileup of TDs of  $C_i^l$  twin at the  $C_{i+3}^{ll}$  twin boundaries is calculated by using CP-FFT, revealing that  $T_i^l$  and  $T_{i+1}^l$  have the largest RSS among six  $\{10\overline{1}2\}$  twin variants.

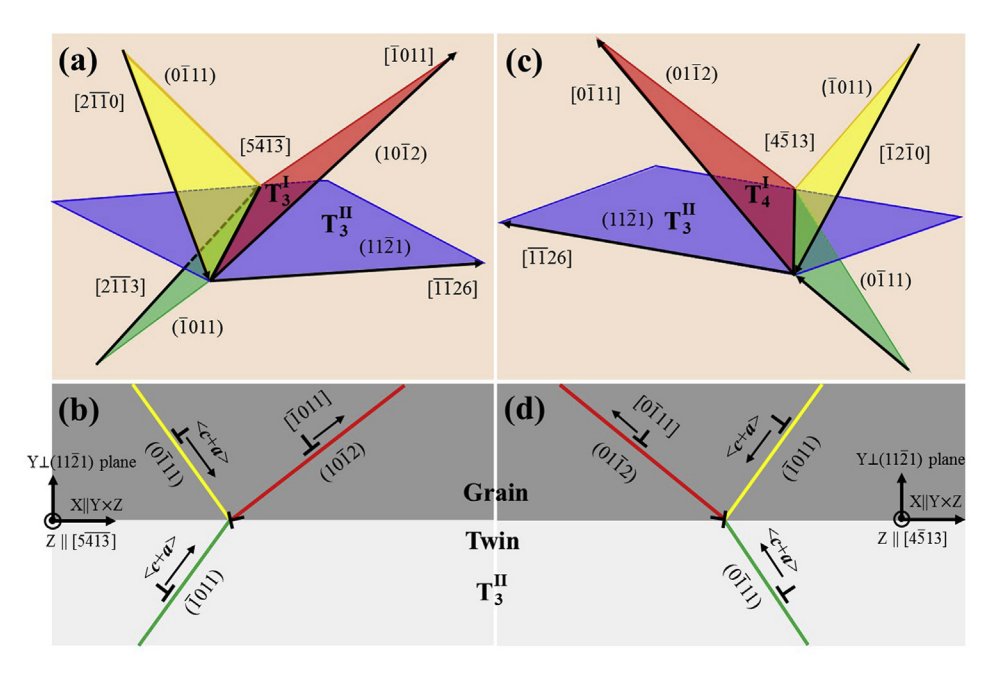


Fig. 8. (a) Illustration of the common line along  $[5\overline{4}\overline{1}\overline{3}]$  among a  $\{10\overline{1}1\}$  pyramidal plane (yellow) in the grain, a  $T_3^{II}$  twinning plane (blue), a  $T_3^{II}$  twinning plane (red) and a  $\{10\overline{1}1\}$  pyramidal plane (green) in the  $T_3^{II}$  twin. (b) Schematic of the reaction of a pyramidal  $\langle \cdot \mathbf{c} + \mathbf{a} \rangle - \mathbf{d}$  is location in the twin and a primary  $T_3^{II}$  twin boundary, leading to slip transformation into a  $T_3^{II}$  twin dislocation in matrix plus a residual dislocation. (c) Illustration of the common line along  $[4\overline{5}13]$  among a  $[10\overline{1}1]$  pyramidal plane (yellow) in the grain, a  $T_3^{II}$  twinning plane (blue), a  $T_4^{II}$  twinning plane (red) and a  $[10\overline{1}1]$  pyramidal plane (green) in the  $[10\overline{1}1]$  twin. (d) Schematic of the reaction of a pyramidal  $(\cdot \mathbf{c} + \mathbf{a}) - \mathbf{c}$  dislocation in the twin and a primary  $[10\overline{1}1]$  twin boundary, leading to slip transformation into a  $[10\overline{1}1]$  twin dislocation in matrix plus a residual dislocation. (For interpretation of the references to color in this figure legend, the reader is referred to the Web version of this article.)

In summary, shock loading causes complicated twinning processes in Ti and Ti alloys corresponding to complex stresses, multiple twinning modes and twin variants. The important finding is that these twinning processes obey simple crystallographic relations according to deformation accommodation ability. The results from this study can be implemented into meso-/macro-scale crystal plasticity models for predicting mechanical behaviors and texture evolution of polycrystalline aggregates of hexagonal materials.

### Acknowledgments

SX, GSL, MYG and JW acknowledge the support by the US National Science Foundation (NSF) (CMMI-1661686). PZ and DWX thank the financial support by the subject development fund of CAEP (Grant No. 2015B0301070). Numerical analysis was completed utilizing the Holland Computing Center of the University of Nebraska, which receives support from the Nebraska Research Initiative.

#### Appendix A. Constitutive model

Crystal plasticity simulations are performed to calculate the local stress field associated with growth of  $\{11\overline{2}1\}$  and  $\{11\overline{2}2\}$  twin in hexagonal Ti using a spectral method coupled with DAMASK [70–72]. Framework and details for using spectral solvers for crystal plasticity and multi-physics simulations can be found in Ref. [73]. The phenomenological crystal plasticity model proposed by Peirce et al. [74] and adapted in DAMASK is used in this study. The microstructure is parametrized in terms of slip resistance  $g^{\alpha}$  on each slip system. We consider three slip families in hexagonal titanium, namely  $\{0001\}\langle<11\overline{2}0\rangle>$  (basal  $<ab href="abs-ref">a</ar>) and <math>\{10\overline{1}1\}\langle<11\overline{2}3\rangle>$  (pyramidal  $<<{c+a}>$ ). There

are 3, 3 and 12 slip systems on the three slip families respectively. The slip resistances increase asymptotically towards to saturation resistance  $g_{\infty}^{\alpha}$  with shear strain  $\gamma$  through the following relationship [75].

$$\dot{g}^{\alpha} = \sum_{\beta} H_0 (1 - g^{\alpha}/g_{\infty}^{\alpha})^a h_{\alpha\beta} \dot{\gamma}^{\beta} \tag{A1}$$

where fitting parameters  $H_0$  and a are initial hardening slope and hardening exponent respectively, and  $h_{\alpha\beta}$  is interaction hardening coefficient. For simplicity,  $h_{\alpha\beta}$  is set to be one for all interaction hardening, and the initial hardening slope for all slip families are set to be equal. For a given set of current slip resistance, shear strain on each slip system evolves at a rate of

$$\dot{\gamma}^{\alpha} = \dot{\gamma}_0 \left| \frac{\tau^{\alpha}}{g^{\alpha}} \right|^{1/n} sgn(\tau^{\alpha}) \tag{A2}$$

where  $\tau^{\alpha} = \mathbf{S_p} \mathbf{b}^{\alpha \otimes} \mathbf{n}^{\alpha}$  is the resolved shear stress on slip system  $\alpha$ , with  $\mathbf{b}^{\alpha}$  and  $\mathbf{n}^{\alpha}$  being the unit vectors along slip direction and slip plane normal respectively;  $\dot{\gamma}_0$  is the reference shear rate, and n is the strain rate sensitivity.

Thermo-expansion method is used to mimic twinning shear. The characteristic twinning shear  $\gamma_c$  for each twinning mode is expressed as a thermal expansion tensor with one non-zero component corresponding to the twinning shear. The loading rate is controlled by the number of total loading steps (N) and time increment ( $\Delta t$ ), which in turn determines the temperature rate. For instance, if total loading steps N=10 and  $\Delta t=0.001s$ , then loading rate is  $(\gamma_c/N)/\Delta t=\gamma_c\times 100/s$ . Correspondingly, the temperature rate should be set to be 100K/s. Details for using spectral solvers for crystal plasticity and thermal expansion in DAMASK should refer to Ref. [73].

**Table A1**Material parameters for hexagonal titanium used in the crystal plasticity model.

Elastic properties Matrix, twin C11 = 160.0 GPa C12 = 90.0 GPa C13 = 66 C33 = 181.7 GPa C44 = 46.5 GPa	.0 GPa	
Buffer layer C11 = 0.1 GPa C12 = 0.0 GPa C44 = 0.05 GF	<sup>2</sup> a	
CRSS for dislocations $g^{lpha}$	{0001} <<11\overline{20}>	254 MPa
	$\{10\overline{1}0\} \langle <11\overline{2}0\rangle >$	141 MPa
	$\{10\overline{1}1\}\ (<11\overline{23})>$	340 MPa
Saturated CRSS for dislocations $g^{\alpha}_{\infty}$	$\{0001\}\ \langle <11\overline{2}0\rangle >$	568 MPa
	$\{10\overline{1}0\} \langle <11\overline{2}0\rangle >$	1500 MPa
	{10 <u>1</u> 1} (<11 <u>23</u> )>	1500 MPa
Reference shear rate	$\dot{\gamma}_0$	$1 \times 10^{-3}$
Initial hardening strength	$H_0$	15Pa
Hardening exponent	а	2
Hardening coefficient	$h_{lphaeta}$	1
Strain rate sensitivity	n	20

#### References

- E. Kleefisch, Industrial Applications of Titanium and Zirconium, ASTM International, 1981.
- [2] I. Altenberger, R.K. Nalla, Y. Sano, L. Wagner, R.O. Ritchie, On the effect of deep-rolling and laser-peening on the stress-controlled low-and high-cycle fatigue behavior of Ti-6Al-4V at elevated temperatures up to 550 C, Int. J. Fatig. 44 (2012) 292–302.
- [3] A.A. Salem, S.R. Kalidindi, R.D. Doherty, Strain hardening of titanium: role of deformation twinning, Acta Mater. 51 (2003) 4225–4237.
- [4] J. Sun, P. Trimby, F. Yan, X. Liao, N. Tao, J. Wang, Shear banding in commercial pure titanium deformed by dynamic compression, Acta Mater. 79 (2014) 47–58.
- [5] A.S. Khan, R. Kazmi, B. Farrokh, Multiaxial and non-proportional loading responses, anisotropy and modeling of Ti-6Al-4V titanium alloy over wide ranges of strain rates and temperatures, Int. J. Plast. 23 (2007) 931–950.
- [6] P. Oberson, S. Ankem, The effect of time-dependent twinning on low temperature (< 0.25\* Tm) creep of an alpha-titanium alloy, Int. J. Plast. 25 (2009) 881–900
- [7] A. Ghaderi, M.R. Barnett, Sensitivity of deformation twinning to grain size in titanium and magnesium, Acta Mater. 59 (2011) 7824–7839.
- [8] J. Warwick, J. Coakley, S. Raghunathan, R. Talling, D. Dye, Effect of texture on load partitioning in Ti-6Al-4V, Acta Mater. 60 (2012) 4117–4127.
- [9] J.W. Christian, S. Mahajan, Deformation twinning, Prog. Mater. Sci. 39 (1995) 1–157.
- [10] P. Partridge, The crystallography and deformation modes of hexagonal closepacked metals, Metall. Rev. 12 (1967) 169–194.
- [11] M. Yoo, Slip, twinning, and fracture in hexagonal close-packed metals, Metallurgical Transactions A 12 (1981) 409–418.
- [12] M.H. Yoo, J.R. Morris, K.M. Ho, S.R. Agnew, Nonbasal deformation modes of HCP metals and alloys Role of dislocation source and mobility, Metall. Mater. Trans. 33A (2002) 813–822.
- [13] N. Gurao, R. Kapoor, S. Suwas, Deformation behaviour of commercially pure titanium at extreme strain rates, Acta Mater. 59 (2011) 3431–3446.
- [14] K. Amouzou, T. Richeton, A. Roth, M. Lebyodkin, T. Lebedkina, Micromechanical modeling of hardening mechanisms in commercially pure  $\alpha$ -titanium in tensile condition, Int. J. Plast. 80 (2016) 222–240.
- [15] S. Song, G. Gray III, Structural interpretation of the nucleation and growth of deformation twins in Zr and Ti—II. Tem study of twin morphology and defect reactions during twinning, Acta Metall. 43 (1995) 2339–2350.
- [16] S. Xu, M. Gong, C. Schuman, J.-S. Lecomte, X. Xie, J. Wang, Sequential (10-12) twinning stimulated by other twins in titanium, Acta Mater. 132 (2017) 57–68
- [17] D. Chichili, K. Ramesh, K. Hemker, The high-strain-rate response of alphatitanium: experiments, deformation mechanisms and modeling, Acta Mater. 46 (1998) 1025–1043.
- [18] T. Wang, B. Li, M. Li, Y. Li, Z. Wang, Z. Nie, Effects of strain rates on deformation twinning behavior in α-titanium, Mater. Char. 106 (2015) 218–225.
- [19] Y. Guo, H. Abdolvand, T. Britton, A. Wilkinson, Growth of {112 2} twins in titanium: a combined experimental and modelling investigation of the local state of deformation, Acta Mater. 126 (2017) 221–235.
- [20] L. Liang, O.B.H. Duparc, First-principles study of four mechanical twins and their deformation along the c-axis in pure  $\alpha$ -titanium and in titanium in presence of oxygen and hydrogen, Acta Mater. 110 (2016) 258–267.
- [21] L. Capolungo, P.E. Marshall, R.J. McCabe, I.J. Beyerlein, C.N. Tomé, Nucleation and growth of twins in Zr: a statistical study, Acta Mater. 57 (2009) 6047–6056.
- [22] H. El Kadiri, C.D. Barrett, J. Wang, C.N. Tomé, Why are twins profuse in magnesium? Acta Mater. 85 (2015) 354–361.
- [23] G.-D. Sim, G. Kim, S. Lavenstein, M.H. Hamza, H. Fan, J.A. El-Awady,

- Anomalous hardening in magnesium driven by a size-dependent transition in deformation modes. Acta Mater. 144 (2018) 11–20.
- [24] J. Tu, X. Zhang, J. Wang, Q. Sun, Q. Liu, C.N. Tomé, Structural characterization of {10-12} twin boundaries in cobalt, Appl. Phys. Lett. 103 (2013), 051903.
- [25] P. Zhou, D. Xiao, C. Jiang, G. Sang, D. Zou, Twin interactions in pure Ti under high strain rate compression, Metall. Mater. Trans. 48 (2017) 126–138.
- [26] N.E. Paton, W.A. Backofen, Plastic deformation of titanium at elevated temperatures, Metall. Mater. Trans. B 1 (1970) 2839–2847.
- [27] S. Xu, M. Gong, X. Xie, Y. Liu, C. Schuman, J.-S. Lecomte, J. Wang, Crystallo-graphic characters of {11-22} twin-twin junctions in titanium, Phil. Mag. Lett. (2017) 1–13.
- [28] Q. Yu, J. Wang, Y. Jiang, R.J. McCabe, N. Li, C.N. Tomé, Twin—twin interactions in magnesium, Acta Mater. 77 (2014) 28–42.
- [29] J.P. Hirth, J. Lothe, Theory of Dislocations, McGraw-Hill, New York, 1968.
- [30] J. Wang, I.J. Beyerlein, J.P. Hirth, C.N. Tomé, Twinning dislocations on {1011} and {1013} planes in hexagonal close-packed crystals, Acta Mater. 59 (2011) 3990—4001
- [31] J. Wang, L. Liu, C.N. Tomé, S.X. Mao, S.K. Gong, Twinning and de-twinning via glide and climb of twinning dislocations along serrated coherent twin boundaries in hexagonal-close-packed metals, Mater Res Lett 1 (2013) 81–88.
- [32] B.-Y. Liu, J. Wang, B. Li, L. Lu, X.-Y. Zhang, Z.-W. Shan, J. Li, C.-L. Jia, J. Sun, E. Ma, Twinning-like lattice reorientation without a crystallographic twinning plane, Nat. Commun. 5 (2014).
- [33] R.C. Pond, J. Hirth, A. Serra, D. Bacon, Atomic displacements accompanying deformation twinning: shears and shuffles, Mater Res Lett 4 (2016) 185–190.
- [34] J. Wang, S. Yadav, J. Hirth, C. Tomé, I. Beyerlein, Pure-shuffle nucleation of deformation twins in hexagonal-close-packed metals, Mater Res Lett 1 (2013) 126–132.
- [35] F. Frank, LXXXIII. Crystal dislocations.—elementary concepts and definitions, the London, Edinburgh, and Dublin, Philosophical Magazine and Journal of Science 42 (1951) 809–819.
- [36] R. Pond, J. Hirth, Defects at surfaces and interfaces, Solid State Phys. 47 (1994) 287–365.
- [37] Y. Li, Y. Chen, J.C. Walmsley, R. Mathinsen, S. Dumoulin, H.J. Roven, Faceted interfacial structure of {101 1} twins in Ti formed during equal channel angular pressing, Scripta Mater. 62 (2010) 443–446.
- [38] B.M. Morrow, R.J. McCabe, E.K. Cerreta, C.N. Tomé, Observations of the atomic structure of tensile and compressive twin boundaries and twin—twin interactions in zirconium, Metall. Mater. Trans. 45 (2014) 5891–5897.
- [39] L. Wang, Y. Yang, P. Eisenlohr, T. Bieler, M. Crimp, D. Mason, Twin nucleation by slip transfer across grain boundaries in commercial purity titanium, Metall. Mater. Trans. 41 (2010) 421–430.
- [40] Q. Yu, J. Wang, Y. Jiang, R.J. McCabe, C.N. Tomé, Co-zone {-1012} twin interaction in magnesium single crystal, Mater Res Lett 2 (2014) 82–88.
- [41] M. Arul Kumar, I.J. Beyerlein, R.J. McCabe, C.N. Tome, Grain neighbour effects on twin transmission in hexagonal close-packed materials, Nat. Commun. 7 (2016) 13826.
- [42] L. Wang, P. Eisenlohr, Y. Yang, T. Bieler, M. Crimp, Nucleation of paired twins at grain boundaries in titanium, Scripta Mater. 63 (2010) 827–830.
- [43] H. Qin, J.J. Jonas, Variant selection during secondary and tertiary twinning in pure titanium, Acta Mater. 75 (2014) 198–211.
- [44] S. Xu, L.S. Toth, C. Schuman, J.-S. Lecomte, M.R. Barnett, Dislocation mediated variant selection for secondary twinning in compression of pure titanium, Acta Mater. 124 (2017) 59–70.
- [45] S. Xu, M. Gong, Y. Jiang, C. Schuman, J.-S. Lecomte, J. Wang, Secondary twin variant selection in four types of double twins in titanium, Acta Mater. 152 (2018) 58–76.
- [46] P. Zhou, S. Xu, D. Xiao, C. Jiang, Y. Hu, J. Wang, Shock-induced {112 1}→{112 2} double twinning in titanium, Int. J. Plast. 112 (2019) 194–205.
- [47] Q. Yu, Y. Jiang, J. Wang, Cyclic deformation and fatigue damage in singlecrystal magnesium under fully reversed strain-controlled

- tension–compression in the [10-10] direction, Scripta Mater. 96 (2015) 41-44.
- [48] Q. Yu, J. Zhang, Y. Jiang, Direct observation of twinning—detwinning—retwinning on magnesium single crystal subjected to strain-controlled cyclic tension—compression in [0001] direction, Phil. Mag. Lett. 91 (2011) 757—765.
- [49] M. Barnett, O. Bouaziz, L.S. Toth, A microstructure based analytical model for tensile twinning in a rod textured Mg alloy, Int. J. Plast. 72 (2015) 151–167.
- [50] H. Qiao, M. Barnett, P. Wu, Modeling of twin formation, propagation and growth in a Mg single crystal based on crystal plasticity finite element method, Int. J. Plast. 86 (2016) 70–92.
- [51] B. Pang, S. Case, I. Jones, J. Millett, G. Whiteman, Y. Chiu, C. Bronkhorst, The defect evolution in shock loaded tantalum single crystals, Acta Mater. 148 (2018) 482–491.
- [52] K. Hazeli, V. Kannan, O. Kingstedt, G. Ravichandran, K. Ramesh, Deformation Twin Nucleation and Twin Variant Selection in Single Crystal Magnesium as a Function of Strain Rate, 2018, p. 10252, arXiv preprint arXiv:1801.
- [53] H. El Kadiri, J. Kapil, A. Oppedal, L. Hector, S.R. Agnew, M. Cherkaoui, S. Vogel, The effect of twin—twin interactions on the nucleation and propagation of twinning in magnesium, Acta Mater. 61 (2013) 3549—3563.
- [54] I. Beyerlein, R. McCabe, C. Tomé, Effect of microstructure on the nucleation of deformation twins in polycrystalline high-purity magnesium: a multi-scale modeling study, J. Mech. Phys. Solid. 59 (2011) 988–1003.
- [55] J.J. Jonas, S. Mu, T. Al-Samman, G. Gottstein, L. Jiang, É. Martin, The role of strain accommodation during the variant selection of primary twins in magnesium, Acta Mater. 59 (2011) 2046–2056.
- [56] I. Beyerlein, J. Wang, M. Barnett, C. Tomé, Double twinning mechanisms in magnesium alloys via dissociation of lattice dislocations, Proc. R. Soc. A 468 (2012) 1496–1520. The Royal Society.
- [57] M.R. Barnett, Z. Keshavarz, A.G. Beer, X. Ma, Non-Schmid behaviour during secondary twinning in a polycrystalline magnesium alloy, Acta Mater. 56 (2008) 5–15.
- [58] K.D. Molodov, T. Al-Samman, D.A. Molodov, S. Korte-Kerzel, On the twinning shear of {101 2} twins in magnesium—experimental determination and formal description, Acta Mater. 134 (2017) 267–273.
- [59] M. Gong, J.P. Hirth, Y. Liu, Y. Shen, J. Wang, Interface structures and twinning mechanisms of twins in hexagonal metals, Mater Res Lett (2017) 1–16.
- [60] W. Wu, S. Ni, Y. Liu, B. Liu, M. Song, Amorphization at twin-twin intersected region in FeCoCrNi high-entropy alloy subjected to high-pressure torsion, Mater. Char. 127 (2017) 111–115.

- [61] Y. Tsai, C. Lin, W. Lee, C. Huang, J. Yang, Mechanical behavior and microstructural evolution of nanostructured bainite under high-strain rate deformation by Hopkinson bar, Scripta Mater. 115 (2016) 46–51.
- [62] Y.-S. Jung, S. Kang, K. Jeong, J.-G. Jung, Y.-K. Lee, The effects of N on the microstructures and tensile properties of Fe-15Mn-0.6 C-2Cr-xN twinninginduced plasticity steels, Acta Mater. 61 (2013) 6541-6548.
- [63] D. Barnett, J. Lothe, An image force theorem for dislocations in anisotropic bicrystals, J. Phys. F Met. Phys. 4 (1974) 1618.
- [64] B. Reed-Hill, E. Buchanan, Zig-zag twins in zirconium, Acta Metall. 11 (1963)
- [65] M. Gong, S. Xu, Y. Jiang, Y. Liu, J. Wang, Structural characteristics of {1 012} non-cozone twin-twin interactions in magnesium, Acta Mater. 159 (2018) 65–76
- [66] T. Maiti, P. Eisenlohr, Fourier-based spectral method solution to finite strain crystal plasticity with free surfaces, Scripta Mater. 145 (2018) 37–40.
- [67] K.E.K. Amouzou, T. Richeton, A. Roth, M.A. Lebyodkin, T.A. Lebedkina, Micromechanical modeling of hardening mechanisms in commercially pure  $\alpha$ -titanium in tensile condition, Int. J. Plast. 80 (2016) 222–240.
- [68] J. Wang, Q. Yu, Y. Jiang, I.J. Beyerlein, Twinning-associated boundaries in hexagonal close-packed metals, JOM (J. Occup. Med.) 66 (2014) 95–101.
- [69] M. Knezevic, M. Zecevic, I.J. Beyerlein, J.F. Bingert, R.J. McCabe, Strain rate and temperature effects on the selection of primary and secondary slip and twinning systems in HCP Zr, Acta Mater. 88 (2015) 55–73.
- [70] F. Roters, P. Eisenlohr, C. Kords, D. Tjahjanto, M. Diehl, D. Raabe, DAMASK: the Düsseldorf Advanced MAterial Simulation Kit for studying crystal plasticity using an FE based or a spectral numerical solver, Procedia IUTAM 3 (2012) 3—10.
- [71] P. Eisenlohr, M. Diehl, R.A. Lebensohn, F. Roters, A spectral method solution to crystal elasto-viscoplasticity at finite strains, Int. J. Plast. 46 (2013) 37–53.
- [72] P. Shanthraj, P. Eisenlohr, M. Diehl, F. Roters, Numerically robust spectral methods for crystal plasticity simulations of heterogeneous materials, Int. J. Plast. 66 (2015) 31–45.
- [73] P. Shanthraj, M. Diehl, P. Eisenlohr, F. Roters, D. Raabe. Spectral Solvers for Crystal Plasticity and Multi-physics Simulations.
- [74] D. Peirce, R. Asaro, A. Needleman, An analysis of nonuniform and localized deformation in ductile single crystals, Acta Metall. 30 (1982) 1087–1119.
- [75] C. Zambaldi, Y. Yang, T.R. Bieler, D. Raabe, Orientation informed nanoindentation of α-titanium: indentation pileup in hexagonal metals deforming by prismatic slip, J. Mater. Res. 27 (2012) 356–367.